The end-Cretaceous in the southwestern Tethys (Elles, Tunisia): orbital calibration of paleoenvironmental events before the mass extinction

Nicolas Thibault, Bruno Galbrun, Silvia Gardin, Fabrice Minoletti, Laurence Le Callonnec

International Journal of Earth Sciences 2015
DOI: 10.1007/s00531-015-1192-0

The end-Cretaceous in the southwestern Tethys (Elles, Tunisia): orbital calibration of paleoenvironmental events before the mass extinction

Nicolas Thibault[1], Bruno Galbrun[2], Silvia Gardin[3], Fabrice Minoletti[2] and Laurence Le Callonnec[2]

(1) IGN, University of Copenhagen, Øster Voldgade 10, 1350 Copenhagen K, Denmark
(2) Institut des Sciences de la Terre Paris (ISTeP), UMR 7193, UPMC Univ Paris 06, Sorbonne Universités, 75005 Paris, France
(3) Centre de Recherche sur la Paléobiodiversité et les Paléoenvironnements, UMR 7072, UPMC Univ Paris 06, Sorbonne Universités, 75005 Paris, France

Nicolas Thibault Email: nt@ign.ku.dk

Abstract
An integrated study of magnetic mass susceptibility (MS), bulk stable isotopes and calcareous nannofossil paleoecological changes is undertaken on the late Maastrichtian of the Elles section, Tunisia, spanning the last ca. 1 Myr of the Cretaceous. A cyclostratigraphic analysis reveals the presence of Milankovitch frequencies and is used for proposal of two distinct orbital age models and to provide ages of important stratigraphic horizons, relative to the age of the Cretaceous–Paleogene boundary (K–PgB). Principal component analysis (PCA) performed on the nannofossil assemblage reveal two main factors, PCA1, mostly representing fluctuations of *D. rotatorius*, *P. stoveri*, *Lithraphidites* spp., *Retecapsa* spp., *Staurolithites* spp., *Micula* spp., and PCA2, mostly representing fluctuations of *A. regularis*, *C. ehrenbergii*, *Micula* spp., *Rhagodiscus* spp., *W. barnesiae* and *Zeugrhabdotus* spp. Variations in PCA1 and PCA2 match changes in bulk $\delta^{13}C$ and $\delta^{18}O$, respectively, and suggest changes in surface-water fertility and temperatures and associated stress. The variations in abundances of high-latitude taxa and the warm-water species *Micula murus* and in bulk $\delta^{18}O$ delineate fast changes in sea-surface paleotemperatures. As in many other sites, an end-Maastrichtian greenhouse warming is highlighted, followed by a short cooling and an additional warm pulse in the last 30 kyr of the Maastrichtian which has rarely been documented so far. Orbital tuning of the delineated climatic events is proposed following the two different age models. Calcareous nannofossil assemblages highlight a decrease in surface-water nutriency, but their species richness remains high through the latest Maastrichtian, indicating, in Tunisia, a weak impact of Deccan volcanism on calcareous nannoplankton diversity before the mass extinction.

Keywords
Late Maastrichtian Cyclostratigraphy Calcareous nannofossils Paleoecology Stable isotopes

Introduction

The Cretaceous–Paleogene boundary (K–PgB) mass extinction and associated paleoenvironmental perturbations have been extensively studied with increasingly high resolution (Abramovich et al. *2010*; Bralower et al. *2010*; Jiang et al. *2010*; Schulte et al. *2010*; Hull et al. *2011*; Alegret et al. *2012*). The last 500 kyr of the Cretaceous is particularly critical as they are characterized by a global greenhouse warming event, most likely linked to Deccan CO_2 degassing, followed by a short cooling interval immediately preceding the K–PgB (Li and Keller *1998a*, *b*; Abramovich and Keller *2002*, *2003*; Nordt et al. *2003*; Wilf et al. *2003*; Thibault and Gardin *2010*). Several perturbations in foraminiferal and calcareous nannofossil assemblages have been recorded in association with this intense warming (Kucera and Malmgren *1998*; Olsson et al. *2001*; Abramovich and Keller *2002*, *2003*; Thibault and Gardin *2010*). Central Tunisia (southwestern Tethys ocean) is of particular importance to address these issues because of its well-exposed K–PgB sections that have a good continuity and are considered as the most biostratigraphically complete records, such as the El Kef global stratotype section and point (GSSP) (Molina et al. *2006*, *2009*). The Elles section, situated 75 km southeast of El Kef (Fig. 1), has also been intensively studied for calcareous nannofossils, foraminifers, stable isotopes, clay mineralogy, Sr/Ca variations and the potential expression of orbital cyclicities (Gardin *2002*; Adatte et al. *2002*; Stüben et al. *2003*). However, past changes in sea-surface-water temperatures have not been clearly demonstrated and paleoenvironmental changes preceding the K–Pg mass extinction lack the precise timing that cyclostratigraphy can nowadays establish (Husson et al. *2014a*). For instance, although orbital cycles have been retrieved from several proxies in the Elles section, these records have not been tuned into the time domain, and the timescale of events preceding the K–PgB was mainly applied based on average sedimentation rates and biostratigraphy (Stüben et al. *2003*). No bulk stable isotope record has yet been published for this section although it bears valuable information in addition to existing stable isotope data on separated benthic and planktic foraminifers (Stüben et al. *2003*). Here, we use high-resolution magnetic susceptibility data to establish a precise orbital calendar of paleoenvironmental events for one of the most complete records of the latest Cretaceous and investigate bulk stable isotopes and calcareous nannofossil assemblages for a potential response to paleoclimatic changes preceding the mass extinction.

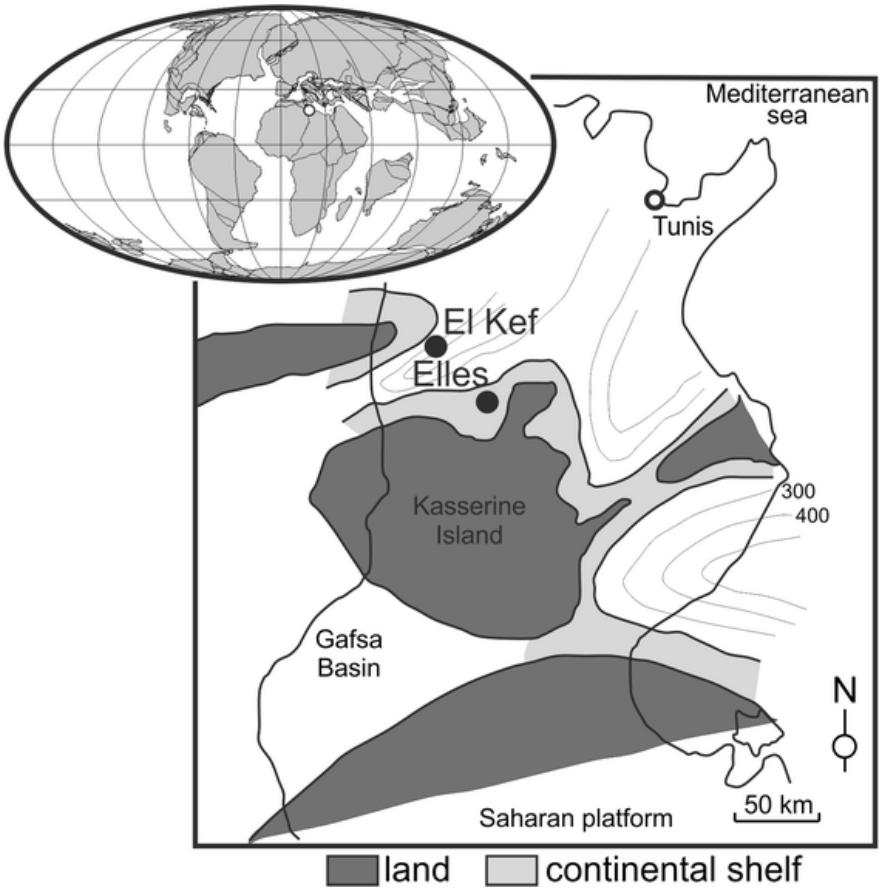

***Fig. 1** : Palaeogeographic position of the Elles section. Modified after Burollet (1967)*

Materials and methods

Paleogeographical setting and lithology of the Elles section

Outcrops of the Elles section, central Tunisia, span a continuous succession from the Campanian to the Eocene. During the Late Cretaceous, the Elles section was situated on the epicontinental shelf of the emerged Kasserine island (Burollet *1967*, Fig. 1). Paleodepth has been estimated between 100 and 150 m using ostracod assemblages (Peypouquet et al. *1986*). The sedimentology of this section was already described in detail in a number of studies (Said *1978*; Zaghbib-Turki et al. *2000*). Sediments of the studied section belong to the El Haria Formation and can be divided into five main units (Fig. 2):

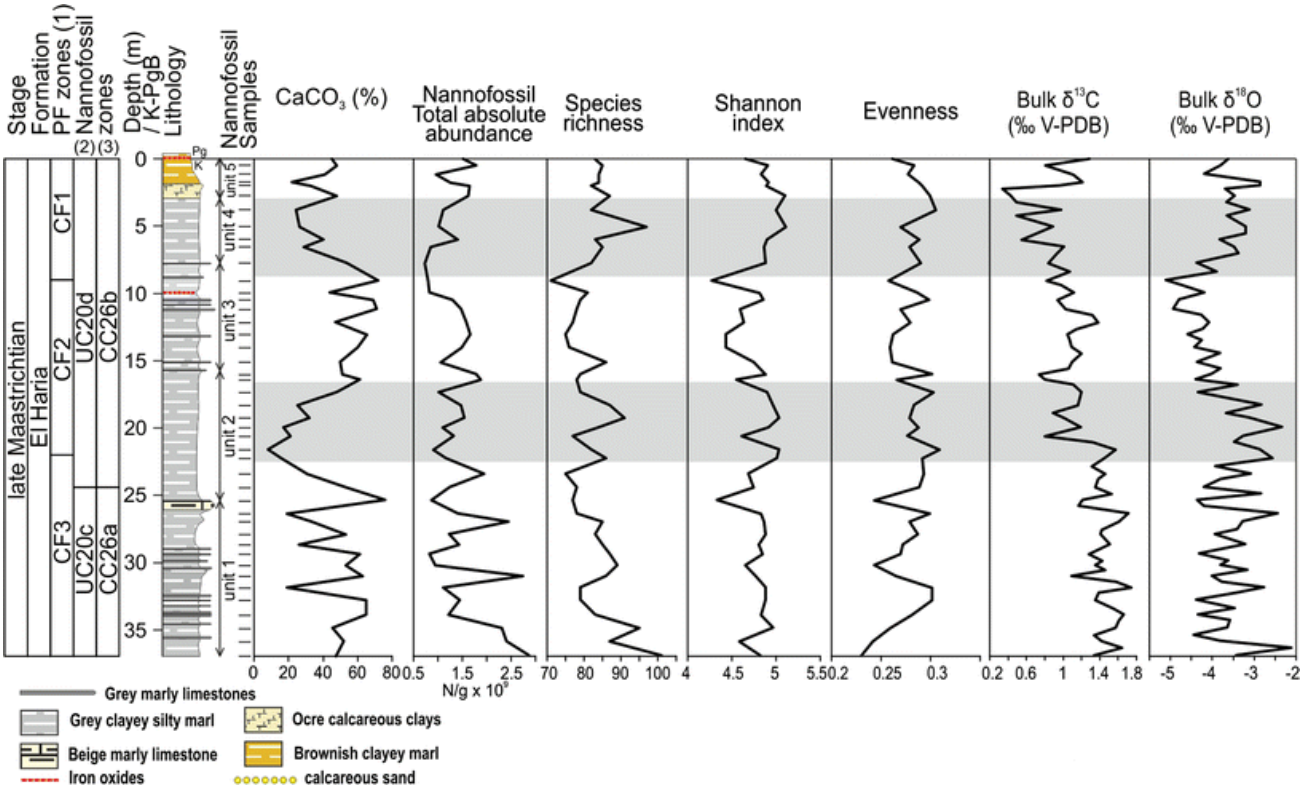

***Fig. 2** : Lithology, calcium carbonate content, total nannofossil abundance, nannofossil diversity indices and bulk oxygen and carbon isotopes of the studied Elles Sect. (1) Planktic foraminifer (PF) zones after Abramovich and Keller (2002). (2) Zonation of Burnett (1998). (3) Zonation of Perch-Nielsen (1985)*

- Unit 1 (−37 to −25.5 m): gray to dark gray silty marls alternating with 5- to 15-cm-thick dark gray marly limestones. The top of this unit is marked by a distinctive 70-cm-thick pale yellow marly limestone bed.
- Unit 2 (−25.5 to −15.75 m): gray silty marls throughout.
- Unit 3 (−15.75 to −7.7 m): gray to pale gray silty marls alternating with 10- to 15-cm-thick dark gray marly limestones. A distinctive reddish level of iron oxides is observed at −10 m. The top of this unit is marked by a millimetric layer of yellow carbonated sand on top of the upper marly limestone bed (Fig. 2).
- Unit 4 (−7.7 to −2.9 m): gray silty marls throughout.
- Unit 5 (−2.9 to 0 m): marked at the base by a distinctive 1-m-thick level of ocre calcareous clays, followed by brownish clayey marls and topped by the reddish clay of the K–Pg boundary, rich in gypsum and iron oxides. In the last 4 cm below the K–Pg boundary, Adatte et al. (2002) noticed, within this unit, a foraminiferal packstone interpreted as a transgressive surface.

Sampling resolution and analysis

Three hundred and forty-nine samples were analyzed for magnetic mass susceptibility (MS) with an average sampling resolution of ca. 15 cm between −37 and −32 m and ca. 10 cm from −32 m onward. Measurements were obtained with a Kappa bridge KLY-2, and the given results correspond to the average of three measurements standardized by the weight of the sample (in 10^{-8} m^3/kg). Magnetic susceptibility measures the capacity of a substance to acquire magnetization when submitted to an external magnetic field. It is commonly used for

cyclostratigraphy in many marine sedimentary records because high-frequency MS variations are directly related to the relative terrigenous supply which is controlled by orbitally forced variations in insolation (Ellwood et al. *2000*).

Oxygen- and carbon-isotopic composition of bulk carbonates were measured with a mass spectrometer Finnigan Delta E on 82 samples (with an average resolution of 50 cm) at the Laboratoire Biominéralisations et environnements sédimentaires (Université Pierre et Marie Curie, Paris 6, France). The extraction of CO_2 was done by reaction with anhydrous orthophosphoric acid at 50 °C. The analytical precision is estimated at 0.1 ‰ for oxygen and 0.05 ‰ for carbon.

For calcareous nannofossil analysis, 44 samples were processed as follows: Sediments were gently disaggregated in a mortar, and 50 mg (M) of dried sediment was weighed and dispersed in 50 ml (V) of distilled water. The suspension was ultrasonicated for 10 s and homogenized with a magnetic stirrer. One milliliter of this suspension was extracted with a finnpipette and homogeneously dropped on a coverslip. Particles are therefore evenly distributed on the coverslip. The coverslip was then mounted on a slide with adhesive. Quantitative counts and estimation of the species richness were performed at a magnification of ×1575 (×63 oil objective with a ×2.5 additional lense). The total nannofossil abundance (number of specimens per gram of sediment, X) was calculated with the following parameters: $X = (N \times S_{cl} \times V)/(S_{fov} \times FOV \times M)$, where N = total number of counted specimens, S_{cl} = surface area of the coverslip (864 mm^2), S_{fov} = surface area of one field of view (0.0172 mm^2), and FOV = total number of investigated fields of view.

In order to record accurately variations in relative abundances of rare to very rare species, the total number of counted specimens was at least 500 for each investigated sample. With this high number of specimens counted, a variation of only 1 % of rare species represents an increase from 5 to 10 specimens observed per slide, which is statistically meaningful (Patterson and Fishbein *1989*). The Shannon–Wiener diversity index was calculated. This index is much used in ecology because it comprises information on both diversity and evenness of the assemblage by taking into account the species richness and the associated relative abundance of each species. Changes in ecological assemblages composed of many species can actually be better described through the classic use of principal component analysis (PCA). This multivariate statistical method simplifies the interpretation of complex datasets with numerous variables by reducing the information contained in the data matrix to a limited number of factors (PCA factors) that express the highest variance in the total assemblage. Prior to the PCA analysis, species were regrouped by taxonomic affinity in order to reduce the number of variables. *Placozygus spiralis* was grouped along with *Zeugrhabdotus* species as *Zeugrhabdotus* spp., and all *Prediscosphaera* were grouped together, except *P. stoveri* which was considered separately because of its high percentage and distinctive changes in abundance. PCA was performed in R-mode on the centered reduced matrix (all abundances standardized by the mean and standard deviation). Calcium carbonate measurements were performed with a carbonate bomb on the same 44 samples processed for nannofossil investigations.

Cyclostratigraphic methods

The cyclostratigraphic analysis was performed on MS variations. Prior to the analysis, data were regularly interpolated at 5 cm and long-term trends were removed from the original signal using a robust loess-smoothing weighted average under Matlab™ over 27 % of the total time series (190 out of a total of 738 data points of the interpolated time series, Figs. 3, 4). Spectral analyses were performed using the multitaper method (MTM, Thomson *1982*) with a red noise simulation from Schulz and Mudelsee (*2002*) developed for Matlab™ by

Husson et al. (*2014b*). The red noise simulation allows the estimation of confidence levels based on a Chi-square statistical test performed on the theoretical spectrum of the red noise. In addition, two running time–frequency spectral tools are used: the wavelet transform using the Matlab™ script of Grinsted et al. (*2004*) and the amplitude spectrogram method developed by Maurer et al. (*2004*), which corresponds to a succession of fast Fourier transform spectral analyses, performed at a constant step along the time series within a sliding window. For analysis in the depth domain, a window of 5 m and a step of 0.1 m were chosen. The resulting amplitude spectrogram thus covers part of the time series only, with 2.5 m (half of the chosen window) being cut away at each edge. In order to extract the potential cyclicities identified by the cyclostratigraphic analysis, we used Taner filters (Taner *2000*) for high-precision extraction of specific astronomical frequency targets. Orbital tuning based on the identification of Milankovitch frequencies was used to provide a relative timescale and to propose ages of nannofossil bio-horizons and previously recorded planktic foraminifer bio-horizons (Abramovich and Keller *2002*). This tuning is only based on the identification of Milankovitch frequencies; calibration to astronomical solutions was not possible here due to the short length of the record. After tuning the time series, the same analyses were performed again in the time domain. The age of relevant biostratigraphic horizons is calculated for two options using an age of 66 Ma for the K–PgB (Kuiper et al. *2008*; Husson et al. *2011*; Renne et al. *2013*).

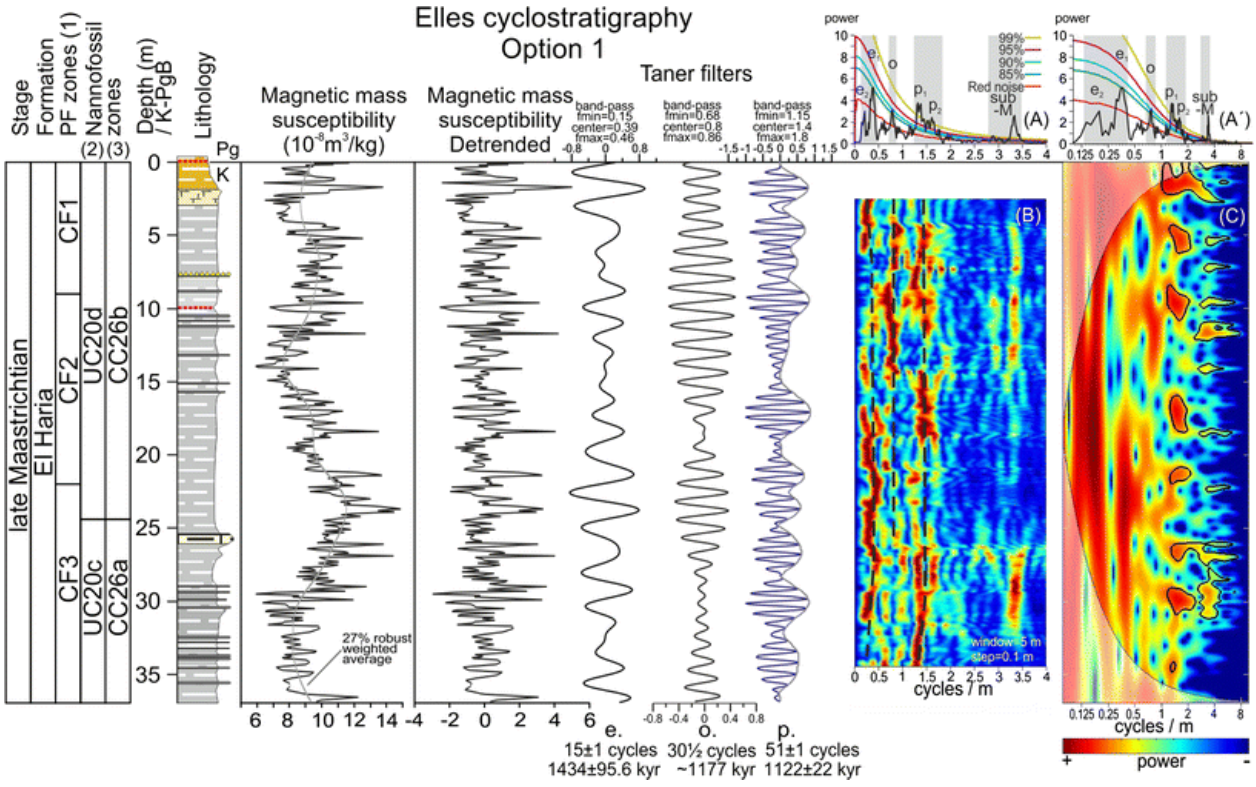

Fig. 3 *:Cyclostratigraphic analysis of the Elles section (option 1).* ***a*** *4π MTM with red noise model and* χ^2 *significance levels.* ***a'*** *Same with a log2 scale on the* x*-axis.* ***b*** *Amplitude spectrogram of the time series.* ***c*** *Wavelet spectrum of the time series.* sub-M *sub-Milankovitch cyclicities*

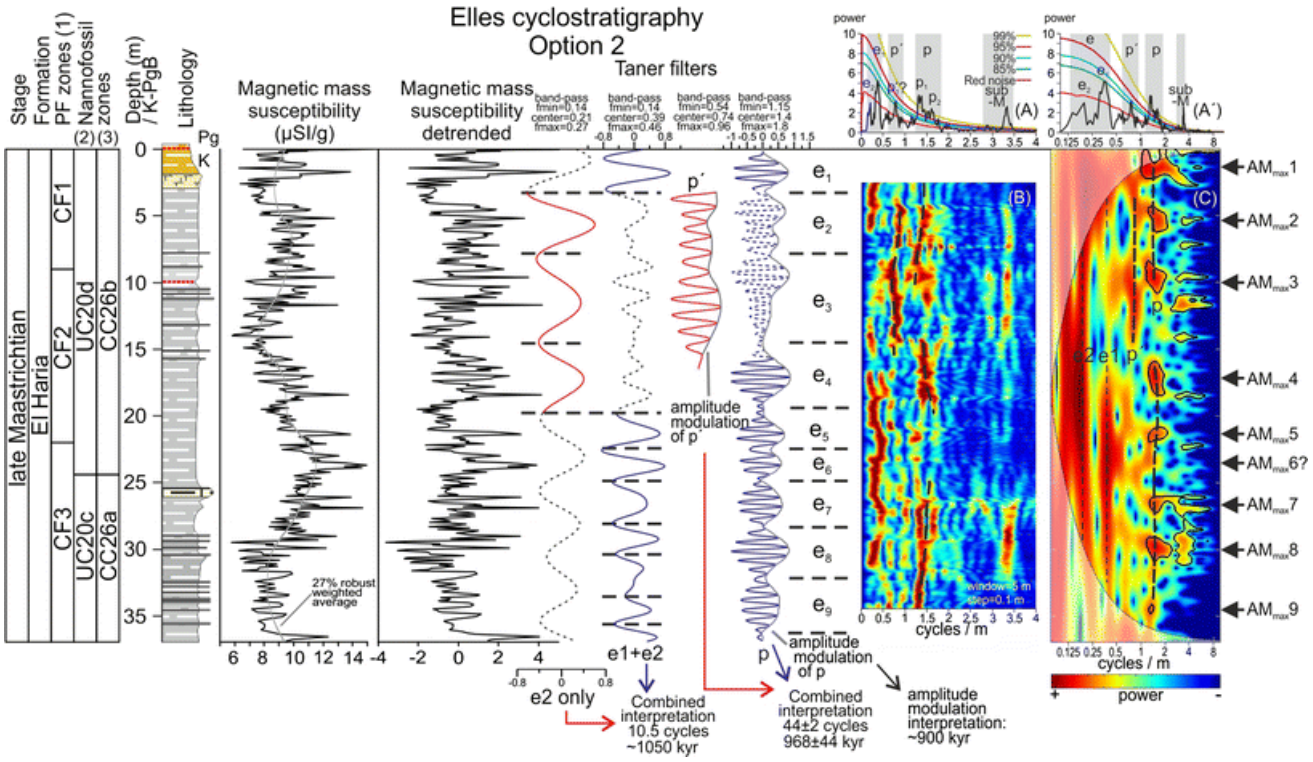

Fig. 4 *:Cyclostratigraphic analysis of the Elles section (option 2).* ***a*** *4π MTM with* red *noise model and* χ^2 *significance levels.* ***a'*** *Same with a log2 scale on the* x*-axis.* ***b*** *Amplitude spectrogram of the time series.* ***c*** *Wavelet spectrum of the time series.* sub-M *sub-Milankovitch cyclicities*

Results

Cyclostratigraphy in the depth domain

Results of the MTM spectral analysis on the detrended MS variations highlight two highly significant frequencies, respectively, centered around 1.35 and 1.6 cycles/m (Fig. 5). Two other peaks reach close to the 90 % significance level at 0.78 and 0.37 cycles/m, whereas a less significant peak can be observed at around 0.22 cycles/m (Fig. 5). An additional highly significant frequency is expressed at 3.4 cycles/m (Figs. 3a, 4a).

(A)

La2004	(kyr)	e2	e1	e3	o2	o1	o3	p1		p2	p3
e2	128	1	0.75	0.59	0.40	0.30	0.23	0.18	0.17	0.14	0.13
e1	95.6	1.34	1	0.79	0.53	0.40	0.30	0.24	0.23	0.19	0.17
e3	76	1.68	1.26	1	0.67	0.50	0.38	0.30	0.29	0.24	0.21
o2	50.6	2.53	1.89	1.50	1	0.75	0.57	0.45	0.43	0.37	0.32
o1	38.2	3.35	2.50	1.99	1.32	1	0.75	0.60	0.57	0.48	0.42
o3	28.8	4.44	3.32	2.64	1.76	1.33	1	0.80	0.76	0.64	0.56
p1	22.9	5.59	4.17	3.32	2.21	1.67	1.26	1	0.95	0.81	0.70
	21.8	5.87	4.39	3.49	2.32	1.75	1.32	1.05	1	0.85	0.73
p2	18.5	6.92	5.17	4.11	2.74	2.06	1.56	1.24	1.18	1	0.86
p3	16	8.00	5.98	4.75	3.16	2.39	1.80	1.43	1.36	1.16	1

(B)

Elles	(m)	e2	e1/e3?	o2	o2?	o1/p´	o3	p1		p2	p3
e2	4.55	1	0.57	0.39	0.36	0.28	0.19	0.17	0.16	0.14	0.13
e1/e3?	2.6	1.75	1	0.68	0.62	0.48	0.33	0.29	0.28	0.24	0.22
o2	1.77	2.57	1.47	1	0.92	0.71	0.49	0.43	0.41	0.35	0.32
o2?	1.62	2.81	1.60	1.09	1	0.78	0.54	0.47	0.44	0.38	0.35
o1/p´	1.26	3.61	2.06	1.40	1.29	1	0.69	0.60	0.57	0.49	0.45
o3	0.87	5.23	2.99	2.03	1.86	1.45	1	0.87	0.83	0.71	0.66
p1	0.76	5.99	3.42	2.33	2.13	1.66	1.14	1	0.95	0.82	0.75
	0.72	6.32	3.61	2.46	2.25	1.75	1.21	1.06	1	0.86	0.79
p2	0.62	7.34	4.19	2.85	2.61	2.03	1.40	1.23	1.16	1	0.92
p3	0.57	7.98	4.56	3.11	2.84	2.21	1.53	1.33	1.26	1.09	1

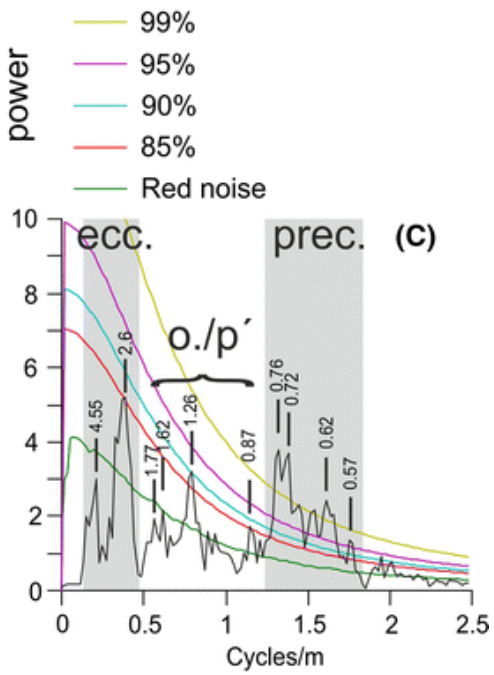

Fig. 5 *: Comparison of frequency ratios between Elles and the La2004 astronomical solution.* ***a*** *Ratios between the main frequency peaks (in kyr) expressed in the La2004 solution for the 66–70 Ma interval. e1, e2, e3, o1, o2, o3 and p1, p2, p3 refer to the peaks of the eccentricity, obliquity and precession by order of importance.* ***b*** *Ratios between the main frequency peaks (in m) expressed in the power spectrum of the Elles section.* ***c*** *4π MTM power spectrum for the Elles section MS measurements*

All those periodicities are significantly highlighted with high powers in the amplitude spectrogram (Figs. 3b, 4b). Within the most significant frequency band centered around 1.5 cycles/m and highlighted in gray (peaks at 1.35 and 1.6, Fig. 3a), regular variations in amplitude are suggested by bifurcations in the amplitude spectrogram (Fig. 3b) and variations in the power of the frequency in the wavelet transform (Fig. 3c). These observations reflect amplitude modulations in this frequency band which is generally characteristic of eccentricity-modulated precession forcing affecting p1 and p2 (Hinnov *2000*; Husson et al. *2014b*). Comparing frequency ratios between the peaks expressed in the power spectrum of Elles and the main significant periodicities of the eccentricity, obliquity and precession expressed in the La2004 astronomical solution (Laskar et al. *2004*) for the 66–70 Ma interval confirm the preceding interpretation and permit the identification of orbital periods in the studied section (Fig. 5). A first interpretation (option 1) points to few variations in sedimentation rate and a simple extraction of the three main well-expressed frequency bands of the eccentricity, obliquity and precession through the use of a band-pass Taner filter (highlighted in gray in Fig. 3). The resulted filter of the eccentricity band is difficult to interpret for cycle counting, presenting several doubtful cycles with very low amplitudes at ca. 7, 15 and 32.5 m (Fig. 3). Cycle counts along this filter may point to 15 ± 1 cycles for the entire section. Cycle counting of the obliquity and precession band filters points, respectively, to 30½ and 51 ± 1 cycles (Fig. 3). While considering the average duration of the main peaks of Milankovitch periodicities of the La2004 solution for the 66–70 Ma interval (Laskar et al. *2004*; Fig. 6), this counting points to a duration of 1434 ± 95.6 kyr for the eccentricity filter, ca. 1177 kyr for the obliquity filter and 1122 ± 22 kyr for the precession filter (Fig. 3). These results point to a

relatively good agreement between the obliquity and precession counting and an offset of more than 200 kyr with respect to the estimation from the eccentricity filter. Three 405 eccentricity cycles would be expected in the long-term trends of the MS signal in line with the previous interpretation. This periodicity is expressed with a high-power peak at ca. 0.07 cycles/m (period of ca. 14 m) on a spectrum performed on non-detrended data. However, periodicities represented by less than 3 cycles in an entire timeseries are very difficult to highlight with precision in a power spectrum (Weedon *2003*). No clear filtering extraction of this periodicity was possible to perform here, but the robust weighted average of the MS signal points to the expression of two long-term cycles only (Fig. 3). The significant frequency centered at 3.3 cycles/m bears a periodicity which is two to three times higher than the sampling resolution. In line with our interpretation, this frequency may correspond to the expression of sub-Milankovitch cycles.

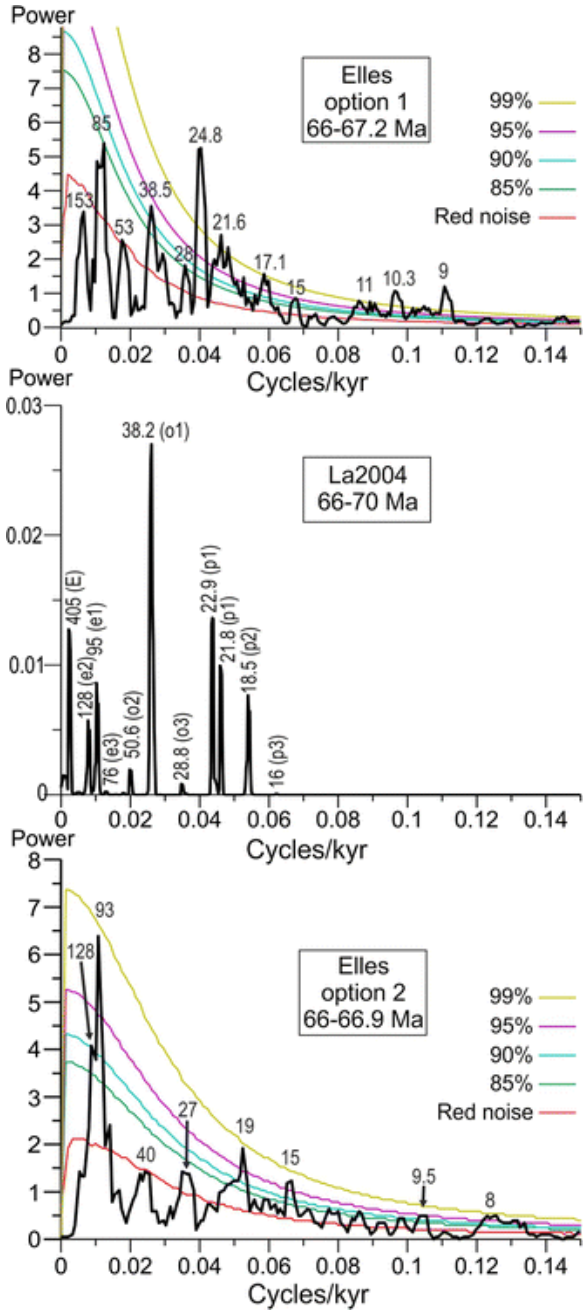

***Fig. 6** : Comparison of 4π MTM power spectra performed in the time domain for options 1 and 2 on the magnetic susceptibility of the Elles section with a 4π MTM power spectrum of the La2004 astronomical solution for the 66 to 70 Ma interval*

Several features of the cyclostratigraphic analysis suggest a different and more complex interpretation of the cyclicity in the Elles record which implies important changes in the sedimentation rate (option 2, Fig. 4). This interpretation relies on the unexpectedly high expression of the obliquity in this low-latitude site and on the expression of amplitude modulations and variations in the power of the different frequency bands in the wavelet and in the amplitude spectrogram (Fig. 4). Within the most significant frequency band centered around 1.5 cycles/m (p1 + p2), regular variations in amplitude are suggested by bifurcations in the amplitude spectrogram (Fig. 4b) and by variations in the power of this frequency in the wavelet transform (Fig. 4c). These variations in the wavelet occur with a wavelength ranging between 2 and 4 m which would correspond to the frequency range of the eccentricity band (e1 + e2) (Fig. 4). These variations reflect amplitude modulations of the 1.5 cycles/m frequency with an average cycle ratio close to 1:5 which is typical of short-eccentricity-modulated precession forcing (Hinnov *2000*). A significant change occurs between −5 and −15 m in the amplitude and wavelet spectrogram with a high-power expression within the frequency band labelled p', previously interpreted as the obliquity in option 1 and centered around 0.79 cycles/m (Fig. 4). Within this interval, the power of p is also significantly lowered and perturbated, and the power of the overall eccentricity band (e1 + e2 on Fig. 4a) is absent in the amplitude spectrogram (Fig. 4b). In option 2, it is assumed that the expression of p' between −5 and −15 m actually corresponds to a sudden shift in the precession band p toward lower frequencies, due a sudden increase in sedimentation rate. In this interval, the disappearance of the eccentricity frequency band from the amplitude spectrogram could then be explained by a shift to a lower frequency corresponding to a period longer than the 5-m window of the analysis (Fig. 4b). In the wavelet spectrogram (Fig. 4c), high power of e1 is also expressed centered at 0.4 cycles/m from 0 to −5 m and from −15 to the base of the section, but this component is poorly significant in the MTM (Fig. 4a) and shows a very low power on the amplitude spectrogram in the interval between −5 and −15 m (Fig. 4b). These results would suggest that an important increase in the sedimentation rate occurred within the −5 to −15 m interval, shifting the significant frequencies to a different range of values. This interpretation can explain the discrepant interpretations in the counting of cycles obtained from the Taner filter of the eccentricity and precession bands in option 1 (Fig. 3). Filtering of the p frequency band results in a signal that presents clear amplitude modulations. These amplitude variations are extracted using a Hilbert transform which highlights the envelope of the filter (Fig. 4). This envelope points to the expression of 9–10 significant cycles only. However, if our recognition of the eccentricity-modulated precession is correct, it is expected to find about 4–6 precession cycles within each of the envelope cycles. This is not the case between −3 and −8 m where only 6 cycles of p can be counted within the 2 envelope cycles (Fig. 4). Therefore, it is likely that the two cycles of the envelope actually correspond to only one eccentricity cycle. Between −8 and −15 m, only one significant cycle is present in the Hilbert envelope of the precession, but this corresponds to about nine cycles of p. This interval corresponds to the perturbated interval described above in the amplitude and wavelet spectrograms, where we suppose a shift in frequencies from p to p′. Therefore, in this interval, the extraction of the precession may actually be better resolved by the p′ filter, while extraction of the eccentricity would be better resolved through extraction of the e2 frequency peak only (Fig. 4). Such an interpretation would respect the average ratio of 1:5 cycles between the precession and eccentricity. Taking all these results into account points to the identification of ca. 10.5 eccentricity cycles while combining the filters of e1 + e2 and e2 only (Fig. 3bis). A total duration of 968 kyr can be calculated from the combination of the p and p′ filters (Fig. 3bis) and nine amplitude modulation cycles named AM1 to AM9 are identified with their maxima highlighted in Fig. 3bis. Option 2 thus points to less discrepancy between the

extraction of eccentricity and precession cycles than in option 1. Option 2 would also be relatively concordant with the two long cycles of the robust weighted average which likely represent the expression of the 405 kyr eccentricity (Fig. 4).

Cyclostratigraphy in the time domain

Cyclostratigraphic analysis in the time domain is fundamental because if the tuning is accurate, then Milankovitch frequencies should be better defined, potentially with higher power in the MTM of the new timeseries. Due to the chaotic behavior of the solar system, the 405 kyr component of the eccentricity is the only orbital parameter stable over the Meso-Cenozoic (Laskar et al. *2004*). In the absence of well-expressed 405 eccentricity cycles in the Elles sedimentary record, the most suitable Milankovitch component for building a cyclostratigraphic time frame should be the obliquity because it is a relatively stable component with a well-defined peak distributed over a very narrow frequency band in the astronomical solution (Fig. 7a).

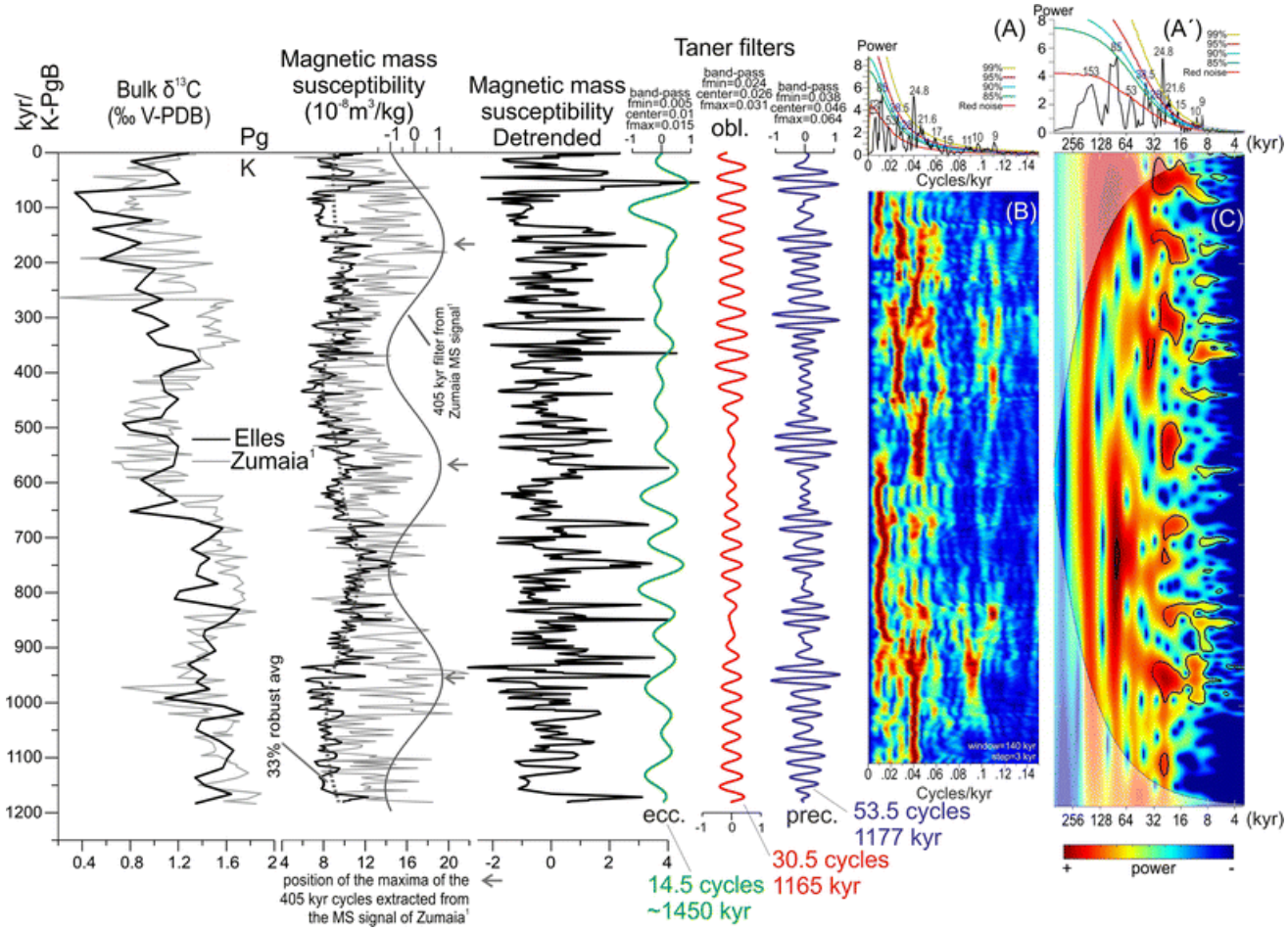

Fig. 7 *: Cyclostratigraphy of the Elles tuned time series in option 1 and comparison with the tuned time series of Zumaia for the bulk $\delta^{13}C$ and magnetic susceptibility (MS). (1) Batenburg et al. (2012).* ***a*** *4π MTM with red noise model and χ^2 significance levels.* ***a'*** *Same with a log2 Scale on the x-axis.* ***b*** *Amplitude spectrogram of the time-series.* ***c*** *Wavelet spectrum of the time-series*

If option 1 is correct, then orbital tuning should be based on the well-expressed obliquity. The tuning into the time domain for option 1 is thus based on the identification of the 30 obliquity

cycles, taking an average duration of 38.2 kyr, corresponding to the expression of this frequency in the La2004 solution (Fig. 6). After the tuning, detrending was performed using a 33 % weighted average. The MTM of the new time series highlights peaks above the 95 % confidence level at 24.8, 21.6, 17.1, 10.3 and 9 kyr (Fig. 7a). The MTM of the tuned time series in option 1 shows an improved expression of the precession and a striking similarity in the period of the obliquity with La2004 (Fig. 6). However, peaks of the eccentricity band remain poorly significant with periods at 153 and 85 kyr which are poorly concordant with the La2004 solution (Fig. 6). While performing a new cyclostratigraphic analysis of the tuned time series based on option 1, the discrepancy in cycle counting remains important between the eccentricity filter and the precession and obliquity filters (Fig. 7). Also, the amplitude spectrogram shows the same perturbations as observed in the depth domain (Fig. 7b).
For option 2, tuning into the time domain was performed based on the identification of the nine amplitude modulation cycles e1 to e9 as highlighted in Fig. 8. The power spectrum of the obtained time series highlights a somewhat reduced power for the expression of the precession, though still significant (Fig. 6). However, this option results in a highly significant and much better expression of the eccentricity with peaks corresponding to periods of 128 and 93 kyr which are concordant with La2004 (Fig. 6). A peak in the obliquity band is also present at 40 kyr but with a low power as expected from a low-latitude site. Also, cyclostratigraphic analysis in the time domain for option 2 shows an amplitude spectrogram and a wavelet with slightly less perturbations, and the power of the eccentricity band remains significant throughout the entire time series within the same frequency band (Fig. 8b, c). Finally, Taner filtering of the precession, obliquity and eccentricity bands in the time domain results in filters that provide similar durations after cycle counting (Fig. 8).

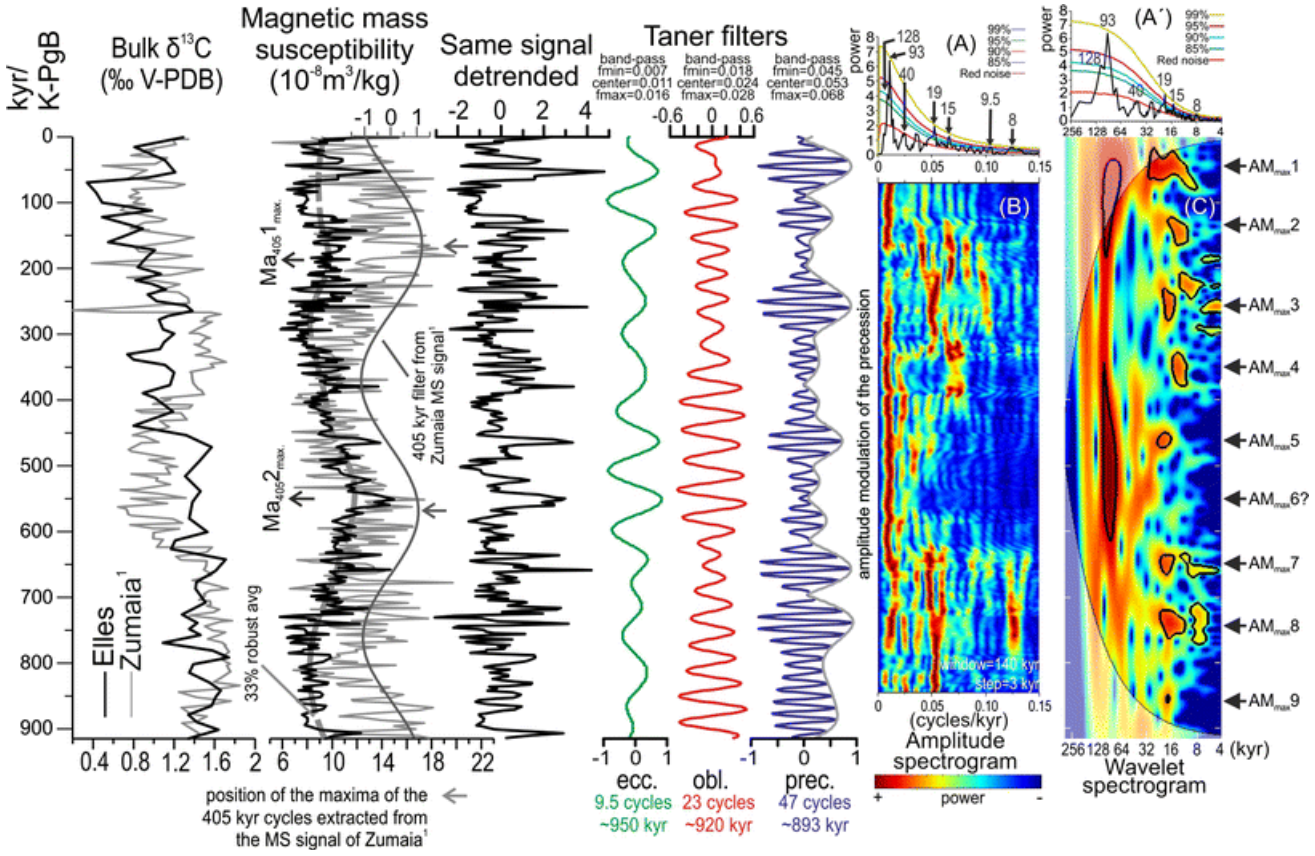

Fig. 8 *: Cyclostratigraphy of the Elles tuned time series in option 2 and comparison with the tuned time series of Zumaia for the bulk $\delta^{13}C$ and magnetic susceptibility (MS). (1) Batenburg*

*et al. (2012). **a** 4π MTM with red noise model and χ^2 significance levels. **a'** Same with a log2 scale on the* x*-axis. **b** Amplitude spectrogram of the time series. **c** Wavelet spectrum of the time series*

Calcium carbonate and stable isotopes

Weight % $CaCO_3$ varies between 8 and 77 % in the investigated samples and reproduces well the five different lithological units described above (Fig. 2). Low values characterize the two homogeneous marly intervals (highlighted in gray in Fig. 2). Higher values and more variability in carbonate content reflect marl–marly limestone alternations in the intervals between −37 and −25.5 m and between −15.75 and −7.7 m. The interval between −2.9 and 0 m also shows slightly higher values than the gray marly interval below.

A cross-plot of carbon and oxygen isotopes is commonly used to test a possible diagenetic overprint which results in a positive correlation between the two ratios (Jenkyns et al. *1995*; Mitchell et al. *1997*). No significant trend is observed on the cross-plot (Fig. 9). Bulk $\delta^{18}O$ values vary between −5.1 and −2.1 ‰. The observed variations also match the observed lithological changes and weight % $CaCO_3$ with somewhat higher values characterizing the homogeneous marly intervals highlighted in gray (Fig. 2). The first interval of alternating marl–marly limestones (−37 to −25.5 m) is characterized by a high variability around of mean of −3.5 ‰. In the homogeneous marly interval above, values oscillate around a mean of −3.1 ‰. The second interval of alternating marl–marly limestones (−15.75 to −7.7 m) is characterized by a negative excursion with values oscillating around a mean of −4.3 ‰ and minimal values reaching −5.1 ‰ between −9 and −11 m. The second interval of homogeneous gray marls is characterized by a positive excursion with values reaching a maximum of −3.1 ‰. A return to more negative values is observed in the three last samples of the studied interval (Fig. 2). Bulk $\delta^{13}C$ values vary between 0.34 and 1.74 ‰. A progressive decrease is observed nearly throughout the section with values reaching the minimum of 0.34 ‰ at −2.2 m within the ocre calcareous clays. From the base of the section to −16.5 m, the decrease in bulk $\delta^{13}C$ appears to be stepwise (Fig. 2). Values sharply increase and reach ca. 1.2 ‰ in the last 2 m before the K–PgB.

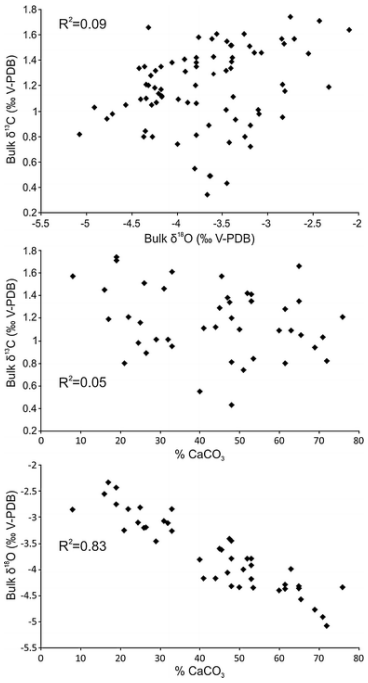

***Fig. 9** : X–Y plot of bulk $\delta^{13}C$ versus bulk $\delta^{18}O$, $\%CaCO_3$ vs bulk $\delta^{13}C$ and $\%CaCO_3$ versus bulk $\delta^{18}O$*

Calcareous nannofossils

Similar to the results previously obtained by Gardin (*2002*), all the investigated samples of the Elles section yielded an abundant, highly diverse and well-preserved late Maastrichtian assemblage. The first occurrence of *Micula prinsii* which defines the base of the CC26b subzone of Perch-Nielsen (*1985*) and the UC20d^{TP} subzone of Burnett (*1998*) was found at −24.4 m, very close to the level identified in Gardin (*2002*). The total nannofossil abundance shows a high variability and the highest recorded values of 2.7×10^9 specimens/g in the first interval of marl–marly limestone alternations (Fig. 2). The species richness is extremely high as compared to other published records of late Maastrichtian nannofossil assemblages, with a minimum of 71 species at −9 m and a maximum of 101 species at the base of the studied interval. The two homogeneous marly intervals are generally characterized by lower values in total nannofossil abundance and somewhat higher species richness. The Shannon index of the nannofossil assemblage is slightly higher in the two marly intervals and exhibit slightly lower values in the second interval of marl–marly limestone alternations and in the last 2.9 m below the K–PgB (Fig. 2).

Four taxa dominate the nannofossil assemblage (Fig. 10): *Micula* spp. (mainly *M. decussata*), *Watznaueria barnesiae*, *Prediscosphaera cretacea* and *Discorhabdus rotatorius*. *Biscutum* spp. have very low abundances, below 1 %. Dominance of solution-resistant taxa *Micula* and *W. barnesiae* in Late Cretaceous assemblages has generally been interpreted as a potential diagenetic overprint in abundance counts (Hill *1975*; Thierstein *1980*). A negative correlation between *Micula* and the total nannofossil abundance and/or between *Micula* and the species richness becomes significant in published successions with various preservations because as preservation worsens, much of the assemblage disappears while the abundance of solution-resistant species (*Micula* and *W. barnesiae*) increases (Roth and Krumbach *1986*; Fisher and Hay *1999*). Such a diagenetic overprint does not appear to have had an important influence on nannofossil assemblages of the Elles section. Because of its small size, *D. rotatorius* is one among the most sensitive species to dissolution and its abundance remains quite high throughout the Elles succession. No change in preservation has been noted in all investigated samples, and there is no significant correlation between *Micula* and the species richness (r^2 Pearson correlation coefficient of 0.22 as compared to a 95 % significance level at 0.26 for 42 degrees of liberty on a one-tailed test). No significant correlation is noted between *Micula* and the total nannofossil abundance (r^2 Pearson correlation coefficient of 0.21). One studied sample at −9 m shows a low nannofossil abundance, the lowest value in species richness and a peak in the relative abundance of *Micula* and *W. barnesiae*. Therefore, this sole sample may potentially be biased by a slight diagenetic overprint, and this is consistent with a minimal value in Bulk $\delta^{18}O$ (Figs. 10, 11). Consequently, the changes observed in the relative abundance of nannofossil species can be interpreted in terms of paleoecological changes.

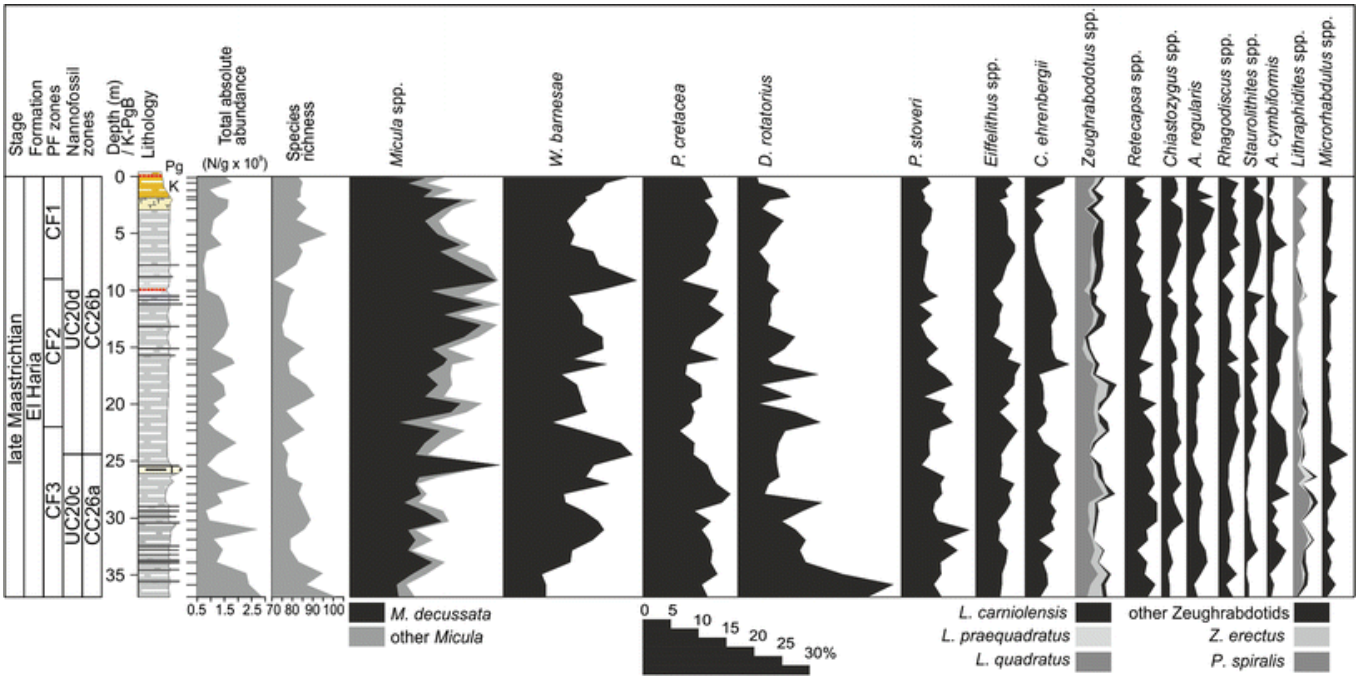

Fig. 10 *: Composition of the nannofossil assemblage in the Elles section*

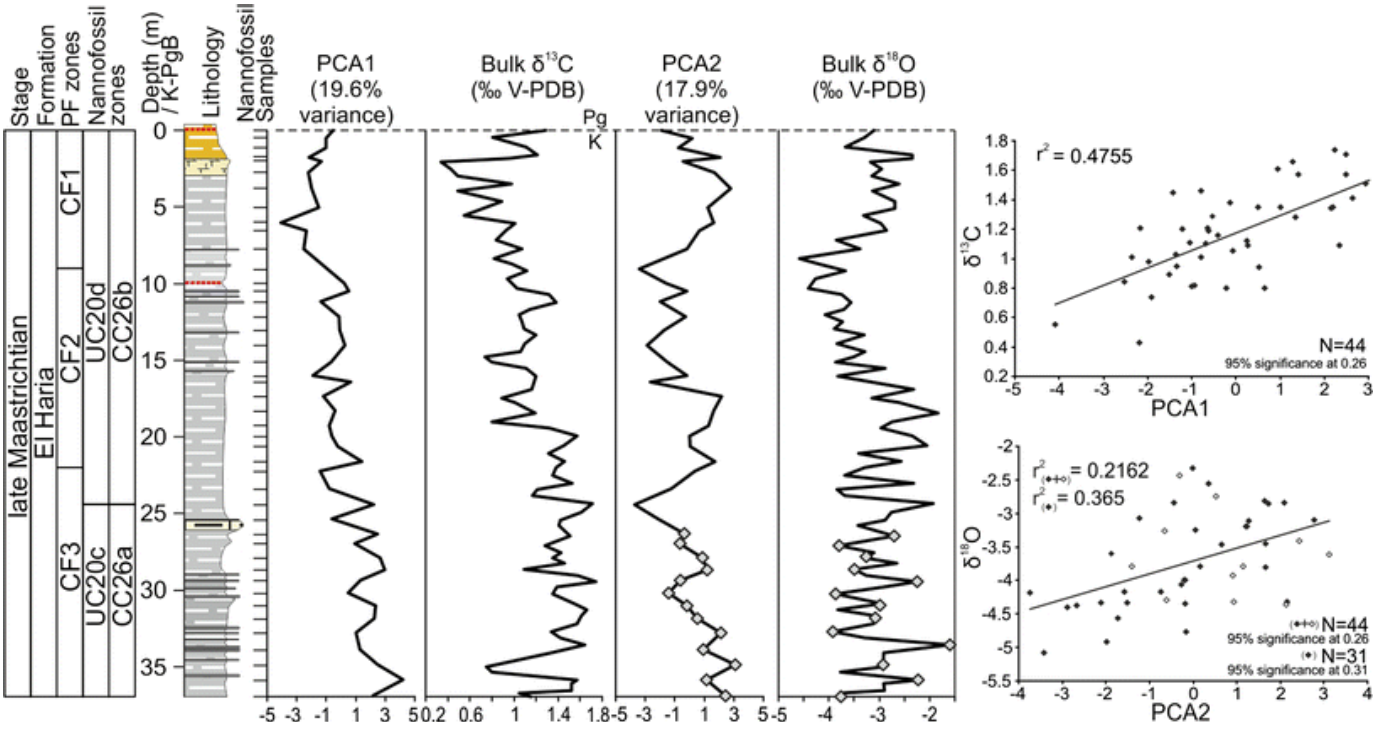

Fig. 11 *: Comparison of PCA factors 1 and 2 with the bulk $\delta^{13}C$ and $\delta^{18}O$*

PCA factor 1 (19.6 % of the variance) is characterized by high positive component loadings of *D. rotatorius*, *Lithraphidites* spp., *P. stoveri* and *Retecapsa* spp. and by high negative component loadings of *Staurolithites* spp. and *Micula* spp. (Table 1). Variations of PCA factor 1 show a progressive decrease from the base of the section to reach a minimum at −6 m. Values remain steadily low in the last 6 m of the Maastrichtian. Although the drop of PCA factor 1 values is not stepwise as for the bulk $\delta^{13}C$, there is a highly significant positive

correlation between these two factors (r^2 of 0.47 as compared to a 95 % significance level of 0.26) (Fig. 11). PCA factor 2 (17.8 % of the variance) is characterized by high component loadings of *Ahmuellerella regularis*, *Zeugrhabdotus* spp. and *Rhagodiscus* spp. and by high negative component loadings of *W. barnesiae*, *C. ehrenbergii* and *Micula* spp. *D. rotatorius* and *Retecapsa* spp appear to have somewhat significant positive and negative loadings to PCA2, respectively (Table 1). Variations in PCA factor 2 highlight the two intervals of homogeneous gray marls by more positive values, and the most negative values are within the interval of marl–marly limestone alternations between −16.5 and −7.7 m. Variations in PCA factor 2 resemble the trends in bulk $\delta^{18}O$, from −24 m to the K–PgB (Fig. 11). A positive trend appears on the x–y plot of PCA2 and the $\delta^{18}O$, but the coefficient of correlation is not significant while taking all data points into account (Fig. 11). This is due to an absence of covariation between the two factors in the interval below −25.5 m (Fig. 11). When discarding data points from the interval below −25.5 m, the correlation coefficient between PCA2 and the $\delta^{18}O$ increases and reaches a value beyond the 95 % significance level, though not really high (Fig. 11).

Table 1 *: Principal component analysis (PCA) factor loadings*

Species	**Group number**	**PCA1 (19.6 % variance)**	**PCA2 (17.8 % variance)**
		Fertility	**Temperature/stress**
A. cymbiformis	N1	0.01	−0.12
A. regularis	N2	−0.16	**0.34**
Chiastozygus spp.	N3	−0.25	0.03
C. ehrenbergii	N4	0.22	**−0.34**
D. rotatorius	N5	**0.34**	0.25
Eiffelithus spp.	N6	−0.18	0.15
Lithraphidites spp.	N7	**0.38**	0.11
Microrhabdulus spp.	N8	0.20	−0.09
Micula spp.	N9	**−0.34**	**−0.29**
Prediscosphaera spp.	N10	0.07	0.19
P. stoveri	N11	**0.30**	0.22
Rhagodiscus spp.	N12	−0.22	**0.29**
Retecapsa spp.	N13	**0.28**	**−0.26**
Staurolithites spp.	N14	**−0.41**	0.14
W. barnesiae	N15	−0.14	**−0.47**
Zeugrhabdotus spp.	N16	0.04	**0.30**

The most significant loadings of each PCA factor are highlighted in bold.

The very high number of specimens counted for each slide allowed the investigation of relative abundance changes of rare to very rare species whose ecology has been well constrained in the past. The relative abundance of the well-established warm-water species *Micula murus* and the sum of cool-water species (Thibault and Gardin *2006*, *2007*, *2010*) is generally below 1 % in samples of the investigated section, but the expanded number of specimens counted to establish variations in the abundance of these taxa allowed the recording of reliable distinctive patterns (Fig. 12). The relative abundance of *Micula murus*

starts increasing slightly at −21.9 m but remains variable and below 0.8 % in the lowermost part of the record (Fig. 12). At −16.2 m, an abrupt increase up to 1.4 % is recorded in concordance with the decrease in bulk $\delta^{18}O$. Values remain higher around 1 % up to −6.5 m where they abruptly drop. The relative abundance of *M. murus* remains low (below 0.3 %) up to −1.5 m where it sharply increases again over 1.5 % in conjunction with a sharp negative peak in bulk $\delta^{18}O$ and lower values in PCA2 (Fig. 12). Cool-water taxa have a very low abundance, generally well below 0.5 % in this southwestern Tethys assemblage. Three intervals with a positive peak in abundance of cool-water taxa can be highlighted at −22.3 m (0.8 %), −20 to −18.5 m (0.9 %) and −5 m (up to 2.5 %). Although these abundances are low, countings were performed over 500 specimens, and such peaks thus represent a meaningful increase from background values where 1–2 specimens only were observed to 4–5 specimens or more. Those three peaks occur in conjunction with higher positive values in PCA2 and the bulk $\delta^{18}O$ (Fig. 12).

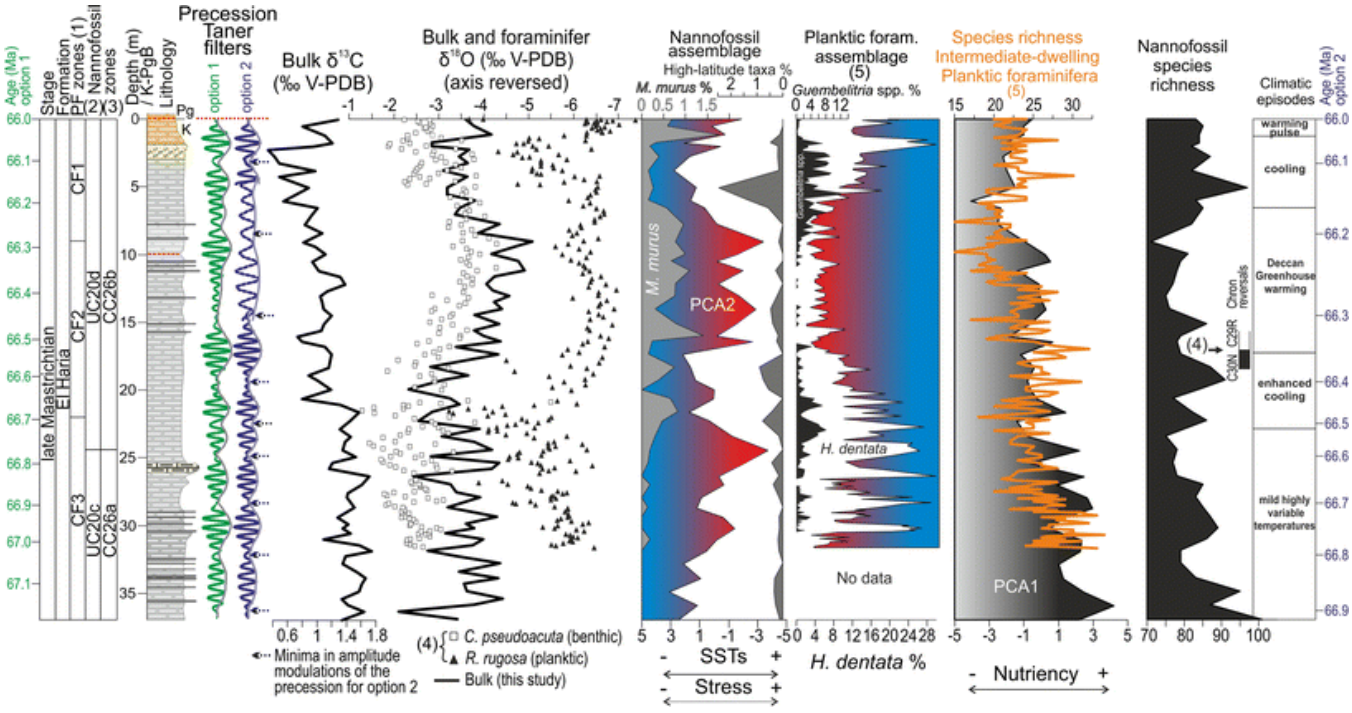

***Fig. 12** : Summary of the main paleoceanographic events during the last 900 kyr of the Cretaceous in the southwestern Tethys. (1) PF zones after Abramovich and Keller (2002). (2) Zonation of Burnett (1998). (3) Zonation of Perch-Nielsen (1985). (4) After Stüben et al. (2003). (5) After Abramovich and Keller (2002)*

Discussion

Validation of the age model and ages of important stratigraphic horizons

The cyclostratigraphic tuning allowed plotting of the $\delta^{13}C$ and MS signals in the time domain for the two different options (Fig. 5bis). Worldwide correlation of bulk carbon-isotopic trends has proved to be a particularly powerful stratigraphic tool for the Maastrichtian stage (Thibault et al. *2012a*, *b*; Voigt et al. *2012*; Wendler *2013*), and a high-resolution reference bulk carbon-isotope curve, tied to an astronomical timescale, is available for the late Maastrichtian of the Zumaia section, Spain (Batenburg et al. *2012*). In addition, MS variations were also measured

with a high resolution at Zumaia and are reported here on the same timescale (in kyr before the K–PgB, Figs. 7, 8). Plotting of the Elles and Zumaia $\delta^{13}C$ and MS records are shown on the same timescale for both options (Figs. 7, 8). None of the two options appears to show a perfect match for either $\delta^{13}C$ or the MS signal, but overall, some of the long-term trends and the range of values of the bulk $\delta^{13}C$ are comparable between Zumaia and Elles. The range of values is clearly different for the MS signal between the two sections, but long-term trends also appear to match with respect to the relative position of minima and maxima in option 2 (Fig. 8). Batenburg et al. (*2012*) found maxima of long-eccentricity cycles $Ma_{405}1$ and $Ma_{405}2$ in the MS signal of Zumaia at 166 and 568 kyr, respectively (Fig. 8). In option 2, these findings match well the interpreted 405 kyr maxima of the 33 % robust weighted average of the Elles MS signal at 187 and 550 kyr for $Ma_{405}1$ and $Ma_{405}2$, respectively (Fig. 8). On the contrary, in option 1, it is rather difficult to reconcile the long-term trends between the two MS signals as a minimum of the Zumaia 405 kyr filter correlates at ca. 750 kyr to a maximum of the 33 % robust average of the Elles MS signal (Fig. 7).

Option 2 is also in agreement with the age-model interpretation of Stüben et al. (*2003*). Biostratigraphic correlations between the Elles section and DSDP Site 525A suggest that the middle of planktic foraminifer zone CF2 corresponds roughly to the base of Chron C29r (Li and Keller *1998b*; Stüben et al. *2003*). The supposed position for the base of Chron C29r obtained through biostratigraphic correlation by the latter authors is reported here in Fig. 12 at ca. −17 m. This level corresponds almost exactly to the base of the negative $\delta^{18}O$ excursion and is only about 1 m below the base of the acme of *Micula murus*, the both events having been proved to be nearly concomitant to the base of C29r in several other sections (Thibault and Gardin *2006*, *2007*, *2010*). The duration of the Cretaceous part of C29r has been constrained through cyclostratigraphy in a number of studies with similar durations ranging between 300 and 370 kyr (Herbert et al. *1995*; Herbert *1999*; Westerhold et al. *2008*; Batenburg et al. *2012*; Husson et al. *2011*, *2014b*). In addition, new U–Pb radiometric datings obtained from intertrappean ash layers in India constrain the base of chron C29r at 66.288 ± 0.027 Ma (Schoene et al. *2015*), whereas the age of the K–Pg boundary has been recently dated at 66.043 ± 0.086 Ma (Renne et al. *2013*). Taking the uncertainties of these two ages into account constrains the duration of the Cretaceous part of C29r to 245 ± 113 kyr. The supposed stratigraphic position for the base of C29r at Elles corresponds to ca. −525 kyr below the K–PgB in option 1 and −350 kyr in option 2 (Fig. 12). Therefore, option 1 falls outside the range of possibilities previously mentioned, whereas option 2 is in accordance with past cyclostratigraphic studies and with the upper range of the estimation obtained from recent radiometric datings.

Ages of important stratigraphic horizons have been derived from the two cyclostratigraphic options (Table 2). Age uncertainties due to the sampling resolution are generally below 5 kyr, except for the FO of *Micula prinsii* (15 kyr). An additional 15 kyr uncertainty is accounted for the slightly discrepant durations of the time series while considering the different filters. These ages are compared to previously published estimations corrected with an age of 66 Ma for the K–PgB (Table 2). The age obtained for the base acme of *Micula murus* fits better to previous estimations in option 2 than in option 1 (Table 2). The age obtained for the FO of *Micula prinsii* points in both options to a very early age as compared to numerous previous records of this bio-horizon near the base of chron C29r, i.e., ca. 350 kyr before the K–PgB (Henriksson *1993*; Thibault and Gardin *2006*, *2007*, *2010*; Gardin et al. *2012*; Thibault et al. *2012b*). However, Hennebert (*2012*) provided an early age of 834 ± 142 kyr before the K–PgB for the FO of *M. prinsii* in the nearby Tunisian Ain Settara section, and Norris et al. (*1998*) reported a very early age of ca. 1 Ma before the K–PgB for this bio-horizon within the upper part of chron C30n in the northwestern Atlantic. In addition, option 1 points to relatively minor changes in sedimentation rate. On the contrary, option 2 points to an increase in sedimentation rate

concomitant to the main negative $\delta^{18}O$ excursion and the increase in *Micula murus*, which is concordant with a strong influence of climate on burial rate (Fig. 13).

Table 2 *: Depth with respect to the Cretaceous–Paleogene boundary and estimated ages of important bio-horizons derived from the cyclostratigraphic analysis at Elles, compared with other published records*
(1) Hennebert (2012), (2) Li et al. (2000), (3) Gardin et al. (2012), (4) Pardo et al. (1996), (5) Thibault and Gardin (2006), (6) Thibault and Gardin (2007), (7) Thibault and Gardin (2010), (8) Norris et al. (1998)

Plankton bio-events	Depth/K–PgB (m)		Age (Ma), K–PgB at 66								
			This study		Ain Settara, Tunisia (1)	El Kef, Tunisia (2)	Italy (3)	Spain (4)	Equatorial Atlantic (5)	South Atlantic (6)	Pacific (7)	Northwest Atlantic (8)
	Top	Bottom	Option 1	Option 2								
FO *P. hantkeninoides* (PF), base CF1	9.6	9.8	66.31 ± 0.002	66.22 ± 0.002	66.25 ± 0.007	~66.3	~66.12	~66.2	–	–	–	–
Base acme *M. murus* (CN)	16	16.4	66.50 ± 0.002	66.33 ± 0.002	–	–	–	–	~66.3	~66.34	~66.34	–
LO *G. gansseri* (PF)	21.4	21.6	66.68 ± 0.002	66.47 ± 0.002	–	–	–	–	–	–	–	–
FO *P. hariaensis* (PF)	21.6	21.8	66.69 ± 0.002	66.48 ± 0.002	–	–	–	–	–	–	–	–
FO *M. prinsii* (CN)	24.4	25.35	66.78 ± 0.003	66.60 ± 0.003	66.83 ± 0.014	–	66.3 ± 0.08	–	~66.3	~66.2	~66.34	~67

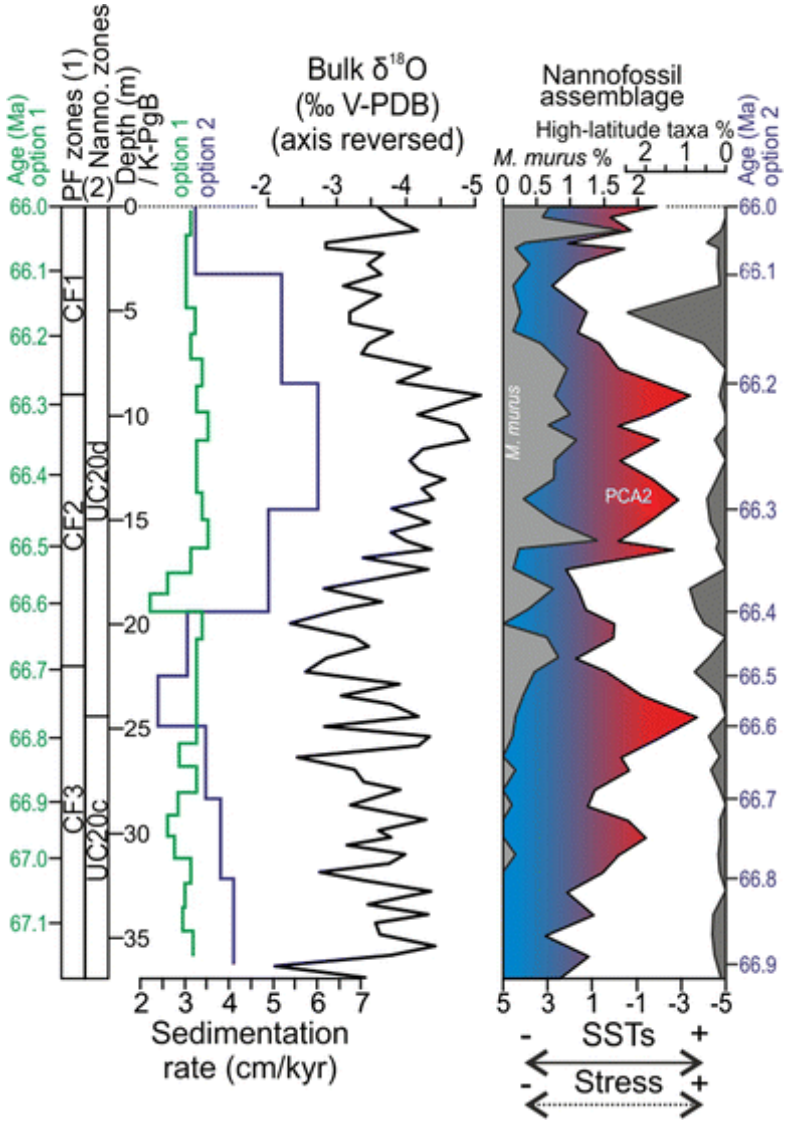

Fig. 13 *: Comparison of the variations in sedimentation rate obtained from the cyclostratigraphic options 1 and 2 with the bulk $\delta^{18}O$ and significant temperatures changes expressed in the calcareous nannofossil assemblage*

Finally, both age models highlight the expression of sub-Milankovitch frequencies which are coherent with semi-precessional cycles (Fig. 6). Similar sub-Milankovitch cycles have been detected throughout the Phanerozoic (Hagelberg et al. *1994*; Rodriguez-Tovar and Pardo-Iguzquiza *2003*; Reuning et al. *2006*; Boulila et al. *2010*; De Vleeschouwer et al. *2012*; Wu et al. *2012*). This periodicity may result from a nonlinear response of the climate system to precession forcing at low latitudes, but the exact nature of these cycles remains a matter of debate (Hagelberg et al. *1994*; Berger and Loutre *1997*; Tuenter et al. *2003*; Berger et al. *2006*; Sun and Huang *2006*; Tuenter et al. *2007*; de Winter et al. *2014*).

Calcareous nannofossil paleoecology and significance of PCA factors

A number of nannofossil taxa have been clearly ascertained as indices of paleotemperature and/or paleofertility of surface waters. In the Late Cretaceous, clear paleobiogeographic distribution patterns and paleoceanographic studies point to a non-questionable affinity of *Ahmuellerella octoradiata*, *Gartnerago* spp., *Kamptnerius magnificus* and *Nephrolithus frequens* to high-latitude cool surface waters (Thierstein *1981*; Lees *2002*), of *Micula murus* to

tropical warm surface waters (Thierstein *1981*; Thibault and Gardin *2006*, *2007*, *2010*), and of *Watznaueria barnesiae* to warm oligotrophic surface waters (Thierstein *1981*; Roth and Krumbach *1986*; Erba et al. *1992*; Williams and Bralower *1995*; Watkins et al. *1996*; Fisher and Hay *1999*; Lees *2002*; Watkins and Self-Trail *2005*; Thibault and Gardin *2007*; Sheldon et al. *2010*). *Biscutum* spp., *Zeugrhabdotus erectus* and *Discorhabdus rotatorius* have been systematically associated with high fertility (Premoli Silva et al. *1989*; Erba *1992*; Erba et al. *1992*; Williams and Bralower *1995*; Fisher and Hay *1999*). In the Maastrichtian of the North German Basin, increasing percentages of *Prediscosphaera stoveri* and *Lithraphidites* spp. were interpreted as reflecting increasing surface-water productivity (Friedrich et al. *2005*). A similar paleoecological affinity was assigned to *P. stoveri* in the late Maastrichtian of the equatorial and south Atlantic (Thibault and Gardin *2006*, *2007*). *Zeugrhabdotus* spp. are considered as mesotrophic taxa (Erba et al. *1992*; Thibault and Gardin *2006*, *2007*; Linnert and Mutterlose *2009*; Linnert et al. *2011*) and appear to show a preference to cool waters (Mutterlose and Kessels *2000*; Tantawy *2008*). *Micula decussata* is a cosmopolitan species whose dominance and increasing abundances have been associated with lowered surface productivity and high-stress environmental conditions (Eshet et al. *1992*; Gardin and Monechi *1998*; Tantawy *2003*; Thibault and Gardin *2006*). However, this taxon is also ten times more resistant to dissolution than any other nannofossil species (Thierstein *1980*). Therefore, interpretation of the abundance trends of this species must be done with caution and careful assessment of the preservation. Neat paleoecological affinities of other Late Cretaceous nannofossil taxa are generally more difficult to establish because many species responded at the same time to temperature and nutriency as well as to potential salinity changes, whereas others were euryoecious taxa with a broad variety of ecological living conditions and opportunistic behavior, increasing in abundance under stressful conditions. The paleoecology of *Cribrosphaerella ehrenbergii*, *Ahmuellerella regularis* and of Maastrichtian representatives of the genera *Retecapsa*, *Staurolithites* and *Rhagodiscus* is poorly constrained. *Cribrosphaerella ehrenbergii* was a cosmopolitan species, common at both low and high latitudes (Lees *2002*). Erba et al. (*1995*) associated blooms of *C. ehrenbergii* in Campanian lagoonal nannofossil assemblages to increased surface-water productivity, whereas Linnert et al. (*2011*) argued that these blooms of *C ehrenbergii* were rather the expression of extreme salinity changes and stressful conditions of lagoonal settings. Linnert et al. (*2011*) argued instead for an oceanic affinity of *C. ehrenbergii* and showed a negative correlation between this species and fertile taxa. The paleoecology of *Ahmuellerella regularis* has never been discussed so far. This cosmopolitan species is rare to frequent at both low and high latitudes (Lees *2002*). *Ahmuellerella octoradiata*, the sister species of this genus, is, however, a cool-water taxon (Thierstein *1981*; Lees *2002*). Elevated abundances of *Retecapsa* spp. were observed in both high and low-fertility settings (Hardas and Mutterlose *2007*; Tiraboschi et al. *2009*; Linnert et al. *2010*, *2011*). Linnert et al. (*2011*) thus consider this taxon as euryoecious, whose abundance is mainly controlled through the competition with other taxa, possibly increasing at times of stressful conditions when the nutrient content is either very low or elevated. In the Cenomanian-Turonian, *Staurolithites crux* is considered as a mesotrophic species (Hardas and Mutterlose *2007*, Hardas et al. *2012*), but this taxon is generally absent in the Maastrichtian and other representatives of the *Staurolithites* genus are rather considered as low-productivity indicators (Eshet and Almogi-Labin *1996*). Valanginian to Late Cenomanian representatives of *Rhagodiscus* (mainly *R. asper*) have been associated with sea-surface warming (Mutterlose *1991*, *1992*; Kessels et al. *2006*; Hardas et al. *2012*), but the paleoecology of Turonian to Maastrichtian *Rhagodiscus* species has never been discussed so far and remains unconstrained.

In light of the literature, the establishment of nannofossil temperature and fertility indices is strictly dependent on the environmental setting in which species were thriving and cannot

always be applied the same way in different paleoenvironmental situations and time slices (Lees et al. *2005*). Although PCA analysis is an objective statistical method that helps extracting potential paleoecological information from the studied assemblage, the results obtained here are not completely straightforward as fertility, temperature, salinity and stressful conditions may sometimes covary. The low-fertility species *Prediscosphaera cretacea* (Eshet and Almogi-Labin *1996*; Hardas et al. *2012*) constitutes 10 to 15 % of the assemblage but shows no significant changes through the profile and low loadings on the PCA axis. This species is not particularly affected by environmental changes in the Elles section (Fig. 10). High positive loadings of *D. rotatorius*, *Lithraphidites* spp. and *P. stoveri* accompanied by high negative loadings of *Staurolithites* spp. and *Micula* spp. to PCA1 suggest that this factor mainly represents variations in the fertility of surface waters (Table 1; Fig. 14). Very high negative loadings of *W. barnesiae* to PCA2 may suggest here a strong influence of surface-water warming as the abundance of this taxon does not appear to be related to fertility factor PCA1 (Fig. 14). Contrariwise, high positive loadings of *A. regularis* and *Zeugrhabdotus* spp. may thus account for surface-water cooling (Fig. 14). However, the significant negative loadings of *C. ehrenbergii* and *Micula* spp. and to a lesser degree of *Retecapsa* spp. to PCA2 suggest that this factor is not only controlled by temperature but also shows a response to environmental stress (Fig. 14). Low values in PCA2 are thus interpreted here as a complex response of the calcareous nannofossil assemblage to increasing environmental stress accompanying surface-water warming. This interpretation may also explain why the correlation between PCA2 and the bulk $\delta^{18}O$ is not completely straightforward, particularly in the interval below −25.5 m (Fig. 11). The significant positive loadings of *Rhagodiscus* spp. to PCA2 may suggest that this species preferred either cooler waters or was unable to compete with other species during periods of environmental stress accompanying the warming (Fig. 14). The correlation between PCA2 and the bulk $\delta^{18}O$, the negative correlation between the long-term trends of PCA2 and the relative abundance of the warm-water *Micula murus* from −20 m to the K–Pg boundary, as well as the three positive peaks in cool-water taxa observed in conjunction with higher positive values in PCA2 and in the bulk $\delta^{18}O$ suggest a control of this factor by surface-water temperature (Fig. 12).

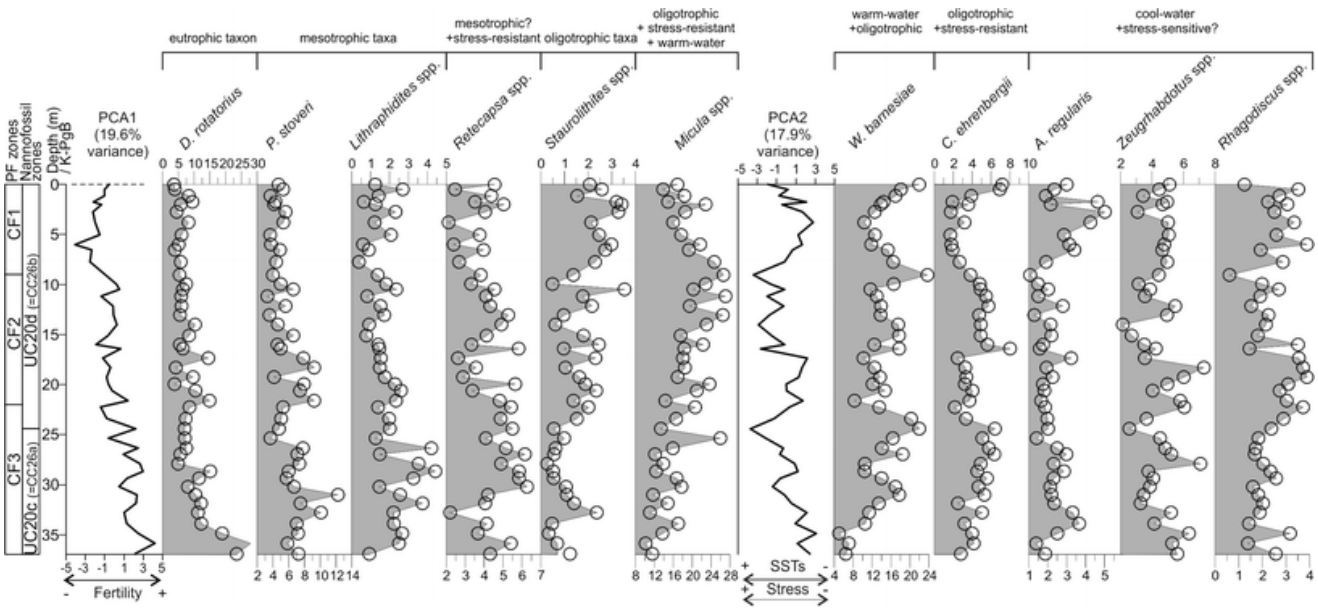

***Fig. 14** : Comparison of PCA factors 1 and 2 with the relative abundance of the most abundant calcareous nannofossil taxa with their inferred paleoecological preferences*

Paleoceanographic significance of isotopic signals

Stable isotopes performed on separated monospecific benthic and planktic foraminifers have long been favoured in paleoceanography over analyses of the bulk carbonate which represents a mixed signal (Grossman *2012*). Geochemical information recorded by bulk carbonate must, however, not be neglected. As noted above, the calcareous nannofossils of Elles are abundant, well-preserved and present relatively few overgrown calcite of diagenetic origin. Calcareous rhombs of early diagenetic origin (Minoletti et al. *2004*; Hermoso et al. *2009*) are found in smear slides of the Elles section, but their abundance is extremely low. Given the location of Elles on an epicontinental shelf, the calcareous sedimentation was controlled by three components: calcareous nannofossils, planktic foraminifera and benthic foraminifera. Foraminifera constitute a very small fraction of the total carbonate in upper Cretaceous sediments (D'Hondt *2005*). The contribution of carbonates produced by calcareous nannofossils is strikingly dominant over foraminifers in Elles samples. Complete foraminifer specimens are rather rare, and only few foraminifer fragments (i.e., isolated chambers, juvenile specimens and tests chips exhibiting second-order birefringence colors) are visible in smearslides (<1 specimen per field of view). These findings are in agreement with the dominance of carbonates precipitated by calcareous nannoplankton in the photic zone in latest Cretaceous hemipelagic sedimentation (D'Hondt *2005*; Minoletti et al. *2005*). Isotopic ratios measured on bulk carbonates mainly represent those of calcareous nannofossil fractions as shown by Minoletti et al. (*2005*). Moreover, recent experiments have shown reduced interspecific differences and less offset in stable isotopes of small and large coccoliths with higher ambient carbon availability, which is expected in the seawater of periods with high CO_2 concentrations (Rickaby et al. *2010*; Moolna and Rickaby *2012*). This finding has been confirmed for nannofossil fractions of past greenhouse conditions (Bolton et al. *2012*). Consequently, bulk $\delta^{18}O$ and $\delta^{13}C$ values of well-preserved bulk carbonates may faithfully reflect trends in the primary isotopic composition of the Cretaceous sea-surface water. Bulk carbonate $\delta^{13}C$ and $\delta^{18}O$ values of the nearby El Kef section also correspond closely to values of the fine-fraction composed mainly of calcareous nannofossils (Perch-Nielsen et al. *1982*). Diagenesis cannot be ruled out and may have shifted isotopic values to a slightly more negative range due to potential bottom water component in the very few early diagenetic rhombs observed in our slides. However, the correlation in isotopic variations and observed changes in the nannofossil assemblage suggest that trends are nicely preserved.

The relatively good correspondence of PCA factor 1 with the bulk $\delta^{13}C$ could suggest that the nannofossil assemblage responded to fertility changes, and conversely, that carbon-isotopic trends may be interpreted here in terms of paleoproductivity (Fig. 12). Carbonate $\delta^{13}C$ is mainly controlled by the global carbon cycle, which is in turn controlled by organic carbon burial, the mode of ocean circulation and the contribution into the marine realm of various external carbon species, such as terrestrial, platform-derived C_{org} and dissolved inorganic carbon, atmospheric CO_2 or methane-derived carbon (Kump and Arthur *1999*; Friedrich et al. *2009*; Wendler *2013*). Contrary to numerous earlier intervals of the Mesozoic, the Maastrichtian is not a period of enhanced burial of organic matter as attested by the absence of any globally and/or supra-regionally distributed black shales. An important late Campanian to early Maastrichtian negative carbon-isotope excursion has been explained by a change in the mode of oceanic circulation shifting the main sources of intermediate and deep waters from low to high latitudes (Barrera and Savin *1999*; Friedrich et al. *2009*). This process was achieved by the end of the early Maastrichtian (Barrera and Savin *1999*; Voigt et al. *2013*), but weakening in high-latitude deep-water formation is also suggested in the middle Maastrichtian (Jung et al. *2013*). Therefore, instability in the mode of the global oceanic circulation could also be evoked here for $\delta^{13}C$ variations in the late Maastrichtian. Pulses of

volcanically derived CO_2 associated with Deccan volcanism would have contributed only to very small changes in the isotopic composition of the oceans (Kump and Arthur *1999*). Late Maastrichtian variations in the marine $\delta^{13}C$ of carbonates can thus be explained through changes in the burial of organic matter that may be triggered during the late Maastrichtian through sea-level changes, instability of the mode of oceanic circulation and/or changes in global productivity (Jarvis et al. *2002*, *2006*). The observed late Maastrichtian decrease in $\delta^{13}C$ was previously associated to a global decrease in marine productivity (Li and Keller *1998a*, *b*, Thibault and Gardin *2010*) and a parallel drop in nutriency is expressed in calcareous nannofossil assemblages in the Atlantic and Pacific Oceans (Thibault and Gardin *2006*, *2007*, *2010*). The local drop in nutriency observed in the Elles section thus coincides with similar drops in the Atlantic and Pacific Oceans. These findings support a global decrease in marine productivity as the most likely explanation for the late Maastrichtian global decrease in the marine $\delta^{13}C$ of carbonates, although an influence on this proxy of potential changes in sea level and sources of deep-water formation cannot be entirely ruled out.

Bulk carbonate $\delta^{18}O$ trends agree relatively well with $\delta^{18}O$ data on separated benthic and planktic foraminifers that thrive and calcify in bottom and surface waters, respectively (Fig. 12). Local influence of sea-level change on sedimentation of the Elles section was investigated by Stüben et al. (*2003*) by the use of the calcite/detritus ratio which reflects variations of the detrital influx. A possible influence of freshwater input on bulk and foraminifer $\delta^{18}O$ values cannot be ruled out since periods of higher $\delta^{18}O$ values correspond to lower Ca/detritus ratios suggesting lower sea levels (Stüben et al. *2003*). These authors discarded this hypothesis because variations observed in benthic foraminiferal $\delta^{18}O$ are similar to records of various oceanic basins and thus likely reflect a global climatic signal. An influence of freshwater input on the bulk $\delta^{18}O$ cannot be ruled out here as there is a clear correlation between the carbonate content and the bulk $\delta^{18}O$ of our samples (Fig. 9). Previously published data on foraminifer stable isotopes (Stüben et al. *2003*) yield important results for comparison with the bulk (Fig. 12). Stüben et al. (*2003*) recognized that the low $\delta^{18}O$ values of their planktic foraminifers may point to a non-negligible diagenetic overprint. They suggested, however, that trends may be well preserved. Isolated foraminifer chambers and juvenile foraminifer tests observed in our smear slides of Elles were almost completely filled with large calcite crystals of undoubtedly diagenetic origin. In addition, planktic foraminifer $\delta^{18}O$ is on average 2.5 ‰ more negative than the bulk $\delta^{18}O$ (Fig. 12). The difference between benthic and planktic foraminiferal $\delta^{18}O$ ($\Delta\delta^{18}O$ planktic–benthic) of latest Maastrichtian subtropical South Atlantic DSDP Sites 525 and 528 is of 0.5 ‰ for a paleodepth of 300–500 m (Barrera and Savin *1999*). The average difference between benthic foraminiferal and bulk $\delta^{18}O$ at Elles is of 0.4 ‰ for a paleodepth of 100–150 m (Fig. 12). In contrast, the $\Delta\delta^{18}O$ planktic–benthic of Elles is on average >2 ‰ and up to 4 ‰ which appears quite unrealistic (Fig. 12). As a consequence, it is likely that the $\delta^{18}O$ of planktic foraminifers in the Elles section is strongly affected by diagenesis. This interpretation can explain the large differences in the range of values obtained for the bulk isotopes and for planktic foraminifers but also the lack of match in some of the long-term trends of these two signals such as: (1) the slight positive excursion observed in planktic foraminifer $\delta^{18}O$ concomitant to the most negative values of the bulk between −11 and −8 m (Fig. 12), (2) the negative excursion observed in planktic foraminifer $\delta^{18}O$ between −8 and −4 m concomitant to a progressive increase in the bulk and in benthic foraminifer $\delta^{18}O$ (Fig. 12). Finally, contrary to the trends observed in the planktic foraminifer $\delta^{18}O$, the trends observed in the bulk $\delta^{18}O$ match well those delineated in the benthic foraminifer $\delta^{18}O$, suggesting that the same climatic changes affected in a similar fashion the entire water column (Fig. 12). This finding supports that the benthic foraminiferal $\delta^{18}O$ was not severely affected by diagenesis, contrary to that of planktic foraminifers. It has long been recognized that diagenetic alteration of foraminiferal calcite is much less problematic in

benthic than in planktic foraminifera and that extensive recrystallization of benthic foraminiferal calcite generally results in minimal shifts from primary $\delta^{18}O$ and $\delta^{13}C$ values (Edgar et al. *2013*). Consequently, we believe that the bulk $\delta^{18}O$ signal of Elles reflects much better the primary composition of the photic zone than planktic foraminiferal $\delta^{18}O$ and that the $\delta^{18}O$ gradient between surface and deep waters is much lower than previously suggested from results of Stüben et al. (*2003*). This interpretation is also supported by the shallow setting of the Elles section. However, a small imprint of an early diagenetic bottom water signature and changes in the freshwater input may also have had some influence on bulk $\delta^{18}O$, and although trends appear reliable, neither this proxy nor planktonic foraminifer $\delta^{18}O$ values is likely to represent faithfully primary sea-surface-water values.

Paleoceanographic changes in the southwestern Tethys for the last 900 kyr of the Cretaceous

As discussed above, biostratigraphic correlation of the Elles section to other records favors option 2 as a reasonable interpretation of the cyclostratigraphic analysis. Paleoceanographic changes unravelled from this section are presented in this chapter with respect to the age scale derived from option 2. Combination of the observed trends in PCA2, in the relative abundance of *Micula murus* and high-latitude taxa and in the bulk $\delta^{18}O$ indicates: (1) mild highly variable sea-surface paleotemperatures from 66.9 to 66.52 Ma, (2) an enhanced cooling event between 66.52 and 66.35 Ma, (3) a pronounced warming event between 66.35 and 66.16 Ma, (4) cooling between 66.16 and 66.03 and (5) a short warming pulse in the last 30 kyr of the Cretaceous (Fig. 12). The highly variable climatic interval at the base of the section is characterized by a high variability in the nannofossil total abundance. Within the two pronounced cooling episodes, nannofossil total abundance is lower and species richness is higher (Fig. 2). This could indicate that relatively cool climate modes generally favoured more diversified, low growth rate, specialized K-strategists, while warmer climate modes, possibly accompanied with stressful conditions, favoured less diversified, blooming ecologic generalists such as *Micula* spp.

Benthic foraminifer $\delta^{18}O$ data delineate similar trends, whereas planktic foraminiferal $\delta^{18}O$ exhibits slightly different fluctuations, particularly within the last 300 kyr of the Maastrichtian (Fig. 12). This can be explained by a potential diagenetic overprint of planktic foraminiferal values but also by the fact that most planktonic foraminifer species of the Campanian–Maastrichtian occupied a subsurface mixed layer rather than surface waters (Abramovich et al. *2003*). In contrast, most nannofossil species of the Maastrichtian were restricted to surface waters. As is the case in this study, Maastrichtian bulk-rock $\delta^{18}O$ signals of pure nannofossil carbonates and nannofossil fractions that did not undergo intense diagenetic alteration might actually better reflect sea-surface temperatures than the existing record of planktic foraminifera at Elles. The main greenhouse warming event is also marked by a significant drop in the relative abundance of the intermediate-dwelling PF *Heterohelix dentata* (Fig. 12). The drop of this ecologic generalist species has been interpreted as a response to environmental stress accompanying the warming episode (Abramovich and Keller *2002*). Surprisingly, blooms of the opportunistic PF *Guembelitria* spp. occur at Elles within the cooling events at 66.52–66.35 Ma and at 66.16–66.03 Ma (Fig. 12).

Important changes in nutriency of the water column occured during the last 900 kyr of the Maastrichtian. A decrease in PCA1 is indicative of a drop in surface-water nutriency from 66.9 to 66.16 Ma (Fig. 12). This is accompanied by a stepwise, progressive decrease in bulk $\delta^{13}C$ from 66.9 to ca. 66.03 Ma. A return to slightly more positive values of the fertility index occurs in the last 160 kyr of the Maastrichtian, whereas the bulk $\delta^{13}C$ returns to more positive values only in the last 50 kyr before the K–PgB. The overall good coupling between the two

parameters and their similarity to contemporaneous records of other oceanic basins (Li and Keller *1998a*, *b*, Thibault and Gardin *2006*, *2007*, *2010*) suggests that the drop of marine primary productivity was the main controlling factor for variations in carbon isotopes. The trends in PCA1 parallel trends in the species richness of PF intermediate dwellers (Fig. 12). The diversity of surface and deep-dweller groups of PFs was relatively unaffected by climatic and productivity changes at Elles (Abramovich and Keller *2002*). As suggested by these authors, PF intermediate dwellers may have been much more sensitive to changes in the nutriency of the water column because they inhabit the thermocline layer where food supply is generally the highest due to the recycling of nutrients from deeper waters. The parallel trends in PCA1 and the diversity of PF intermediate dwellers could thus be explained by changes in the depth of the nutricline layer. However, there is no clear link between fertility/intermediate dweller species richness and temperature changes. The first two coupled parameters remain relatively stable during the lower half of the end-Cretaceous warming and drop abruptly to reach minimum values at the transition between the warming and the following cooling event (Fig. 12). Therefore, in the Elles section, minima in surface-water nutriency and maximum stress within the group of PF intermediate dwellers occurred at the transition between the greenhouse warming and the end-Maastrichtian cooling. This episode of stress is also characterized by the increase in the relative abundance of the opportunist *Guembelitria* group (Abramovich and Keller *2002*; Fig. 9) The relationship between nannofossil species richness, climate change and potential ecological stress is not straightforward. Few peaks and somewhat higher values in species richness are recorded during the cooling episodes (Fig. 12). The nannofossil diversity remained on average very high, >80 species until the very end of the Cretaceous.

Replacing the Elles record in a global context

The large increase in PCA2 and the acme of *Micula murus* recorded here at 66.35–66.16 Ma is similar to findings in the Tropical Pacific and in the Atlantic and correlates with the global expression of the end-Maastrichtian warming as expressed in the $\delta^{18}O$ of benthic foraminifera and bulk carbonates (Barrera and Savin *1999*; Thibault and Gardin *2010*). Moreover, this episode correlates with an increase in atmospheric pCO_2 calculated from the $\delta^{13}C$ of paleosol carbonates in Texas (Nordt et al. *2003*; Wilf et al. *2003*). Several of the main biotic changes observed globally at the end of the Maastrichtian in planktic foraminifers are also coincident with this episode of warming. Among these changes, dwarfism of planktic foraminifers and increase in abundance of the opportunist *Guembelitria* group suggest stressful conditions associated with the greenhouse warming within chron C29r of several tropical sections (Abramovich and Keller *2002*, *2003*; Abramovich et al. *2010*). Blooms of the opportunist *Guembelitria* are also observed within biozone CF1, immediately prior to the K–PgB in Texas, Egypt, Israel and India (Keller et al. *2012*; Punekar et al. *2014*). Several authors suggested that the end-Maastrichtian warming was triggered by Deccan volcanism through the addition of greenhouse gas CO_2 to the atmosphere (Dessert et al. *2001*; Wignall *2001*; Cohen and Coe *2002*). Other studies suggested that the impact of SO_2 degassing related to flood basalt volcanism would trigger short-term episodes of intense cooling and strong environmental instabilities (Chenet et al. *2005*; Self et al. *2008*).

There is thus few doubt that phase 2 of Deccan volcanism (the main Cretaceous phase as defined by Chenet et al. *2009*), the end-Maastrichtian greenhouse warming and associated biotic perturbations start concomitantly very close to the C29r/C30n reversal (Li and Keller *1998a*, *b*; Barrera and Savin *1999*; Wilf et al. *2003*; Keller et al. *2008*; Robinson et al. *2009*). The timing of the end-Maastrichtian warming obtained from the cyclostratigraphic interpretation of option 2 at Elles appears concordant with these past studies (Fig. 12). The

short episode of cooling following the Deccan warming was also demonstrated in a number of previous studies (Li and Keller *1998b*; Bernaola and Monechi *2007*; Thibault and Gardin *2007*, *2010*). In the Elles record, cooling starts ca. 160 kyr before the K–PgB, lasts for about 120–130 kyr, and is followed by an additional warming pulse in the last 30 kyr of the Cretaceous (Fig. 12), in accordance with the previous interpretation of Stüben et al. (*2003*) and Punekar et al. (*2014*). This climatic evolution points to very rapid sea-surface temperature changes that could reflect the interplay between CO_2 and SO_2 injections from Deccan volcanism. It is thus likely that the environmental conditions preceding the K–PgB triggered stress and extinctions prior to the bolide impact. Moreover, biotic perturbations seem to have been triggered during both the warming and cooling phases of the last 350 kyr of the Cretaceous (Ward *1990*; Abramovich and Keller *2002*, Keller et al. *2012*; Stinnesbeck et al. *2012*; Tobin et al. *2012*, *2014*). These latter findings probably reflect the difficulty of biotic groups to adapt to these rapid climatic changes. As far as calcareous nannoplankton is concerned, the main changes occur in association with the end-Maastrichtian greenhouse warming. A slight decline in species richness of this group is recorded during this episode in the tropical Pacific and in the South Atlantic (Thibault and Gardin *2010*). However, nannofossil species richness returns to higher values in the following episode of cooling preceding the K–PgB in the Pacific (Thibault and Gardin *2010*). At Elles, the nannofossil species richness remains very high until the end of the Maastrichtian (Fig. 12). As shown in this study and in Thibault and Gardin (*2006*, *2007*, *2010*), calcareous nannofossils highlight a global drop in the nutriency of tropical surface waters in the late Maastrichtian (Fig. 12). However, in the present study and as in many sections worldwide (Pospichal *1996*; Bown *2005*; Jiang et al. *2010*), the climatic fluctuations and environmental perturbations associated with Deccan volcanism had a relatively weak impact on the diversity of the calcareous nannoplankton community prior to the K–PgB bolide impact.

Apparent contradictions in the modelled climatic effects of Deccan volcanism and in the response of different marine biological groups to the associated environmental perturbations point to a very complex scenario for the end-Cretaceous mass extinction. Unravelling the complexity of this scenario in the marine realm will only arise from cross-disciplinary studies of the different groups of the marine biota calibrated with cyclostratigraphy, recent time constraints from radiometric dating of the Deccan lava pile (Schoene et al. *2015*), and the development of geochemical proxies of volcanism in marine sediments.

Conclusions

The integrated study of the Elles section has established a precise calendar of paleoenvironmental events in the southern Tethys for the last 900 kyr preceding the K–PgB:

- The cyclostratigraphic analysis of the Elles section, Tunisia, revealed a strong precessional forcing in MS variations with amplitude modulation by the eccentricity, and a well-expressed obliquity signal, allowing the building of an age model for the latest Maastrichtian of the southwestern Tethys.
- Variations in PCA2, subtle variations in abundances of cool-water taxa and the warm-water species *Micula murus* and variations in bulk carbonate and foraminifer $\delta^{18}O$ point to a common paleoclimatic interpretation in Tunisia. Sea-surface paleotemperatures were generally cooler and highly variable between 66.9 and 66.35 Ma with an enhanced cooling event recorded between 66.52 and 66.35 Ma. A major warming of sea-surface waters is recorded between 66.35 and 66.16 Ma and reflects the expression of the worldwide end-Maastrichtian greenhouse warming. Cooling resumed between 66.16 and 66.03 Ma. The last 30 kyr of the Cretaceous is characterized by an additional short warming pulse.

- The last 900 kyr of the Cretaceous is characterized by a decrease in surface-water nutriency as indicated by the nannofossil assemblage through PCA1. This finding is similar to records of the Atlantic and Pacific Oceans which suggest that the concomitant global decrease in bulk $\delta^{13}C$ could be caused by a drop in overall plankton productivity.
- The species richness of intermediate-dwelling planktic foraminifera (PF) parallels the trends in the nannofossil fertility index, indicating a direct link between the drop in surface-water nutriency and stressful environmental conditions within the nutricline. Maximum stress in PF and minimum nutriency occurred at the transition between the greenhouse warming and the end-Maastrichtian cooling.
- The $\delta^{13}C$, the nannofossil fertility index and the species richness of intermediate-dwelling planktic foraminifera all returned to slightly more positive values during the last 160 kyr of the Cretaceous suggesting a return to less stressful conditions.
- The nannofossil species richness tends to be lower during warming episodes, thus confirming that stressful conditions may have accompanied greenhouse warming pulses. However, the species richness remained very high throughout the last 900 kyr of the Cretaceous.

Acknowledgments
Funding for this study was provided by Eclipse II Program and the Carlsberg Foundation. Warmly thanks to Chokri Yaich and Habib Bensalem for guidance in the field. We are grateful to Thierry Adatte and Christian Linnert for critical review, helpful suggestions and discussions of the manuscript.

Electronic supplementary material
Below is the link to the electronic supplementary material.
Supplementary material 1 (XLSX 48 kb)

References

1. *Abramovich S, Keller G (2002) High stress late Maastrichtian paleoenvironment: inference from planktonic foraminifera in Tunisia. Palaeogeogr Palaeoclimatol 178:145–164*
2. *Abramovich S, Keller G (2003) Planktonic foraminiferal response to the latest Maastrichtian abrupt warm event: a case study from South Atlantic DSDP Site 525A. Mar Micropaleontol 48:225–249*
3. *Abramovich S, Keller G, Stüben D, Berner Z (2003) Characterization of late Campanian and Maastrichtian planktonic foraminiferal depth habitats and vital activities based on stable isotopes. Palaeogeogr Palaeoclimatol 202:1–29*
4. *Abramovich S, Yovel-Corem S, Almogi-Labin A, Benjamini C (2010) Global climate change and planktic foraminiferal response in the Maastrichtian. Paleoceanography. doi:10.1029/2009PA001843*
5. *Adatte T, Keller G, Stinnesbeck W (2002) Late Cretaceous to early Paleocene climate and sea-level fluctuations: the Tunisian record. Palaeogeogr Palaeoclimatol 178:165–196*
6. *Alegret L, Thomas E, Lohmann KC (2012) End-Cretaceous marine mass extinction not caused by productivity collapse. Proc Natl Acad Sci USA 109:728–732*
7. *Barrera E, Savin SM (1999) Evolution of late Campanian-Maastrichtian marine climates and oceans. In: Barrera E, Johnson CC (eds) Evolution of the Cretaceous ocean-climate system. Geol Soc Am S 332:245–282*
8. *Batenburg SJ, Sprovieri M, Gale AS, Hilgen FJ, Hüsing S, Laskar J, Liebrand D, Lirer F, Orue-Etxebarria X, Pelosi N, Smit J (2012) Cyclostratigraphy and astronomical tuning of the*

Late Maastrichtian at Zumaia (Basque country, Northern Spain). Earth Planet Sc Lett 359–360:264–278

9. *Berger A, Loutre MF (1997) Intertropical latitudes and precessional and half-precessional cycles. Science 278:1476–1478*
10. *Berger A, Loutre MF, Mélice JL (2006) Equatorial insolation: from precession harmonics to eccentricity frequencies. Clim Past 2:131–136. doi:10.5194/cp-2-131-2006*
11. *Bernaola G, Monechi S (2007) Calcareous nannofossil extinction and survivorship across the Cretaceous − Paleogene boundary at Walvis Ridge (ODP Hole 1262C, South Atlantic Ocean). Palaeogeogr Palaeoclimatol 255:132–156*
12. *Bolton CT, Stoll HM, Mendez-Vicente A (2012) Vital effects in coccolith calcite: Cenozoic climate-pCO_2 drove the diversity of carbon acquisition strategies in coccolithophores? Paleoceanography. doi:10.1029/2010PA001951*
13. *Boulila S, Galbrun B, Hinnov LA, Collin PY, Ogg JG, Fortwengler D, Marchand D (2010) Milankovitch and sub-Milankovitch forcing of the Oxfordian (Late Jurassic) terres noires formation (SE France) and global implications. Basin Res 22:717–732*
14. *Bown P (2005) Selective calcareous nannoplankton survivorship at the Cretaceous–Tertiary boundary. Geology 33:653–656*
15. *Bralower T, Eccles L, Kutz J, Yancey T, Schueth J, Arthur M, Bice D (2010) Grain size of Cretaceous–Paleogene boundary sediments from Chicxulub to the open ocean: implications for interpretation of the mass extinction event. Geology 38:199–202*
16. *Burnett JA (1998) Upper Cretaceous. In: Bown P (ed) Calcareous nannofossil biostratigraphy. British Micropaleontology Society Publication Series. Chapman & Hall/Kluwer Academic Publishers, London, pp 132–199*
17. *Burollet PF (1967) General geology in Tunisia. In: Martin L (ed) Guidebook to the geology history of Tunisia. Petroleum Exploration Society of Libya, 9th annual field conference, p 67*
18. *Chenet A-L, Fluteau F, Courtillot V (2005) Modelling massive sulphate aerosol pollution, following the large 1783 Laki basaltic eruption. Earth Planet Sci Lett 236:721–731*
19. *Chenet A-L, Courtillot V, Fluteau F, Gerard M, Quidelleur X, Khadri SFR, Subbarao KV, Thordarson T (2009) Determination of rapid Deccan eruptions across the Cretaceous–Tertiary boundary using paleomagnetic secular variation: 2. Constraints from analysis of eight new sections and synthesis for a 3500-m-thick composite section. J Geophys Res Earth 114(B6). doi:10.1029/2008JB005644*
20. *Cohen AS, Coe AL (2002) New geochemical evidence for the onset of volcanism in the Central Atlantic magmatic province and environmental change at the Triassic–Jurassic boundary. Geology 30:267–270*
21. *D'Hondt S (2005) Consequences of the Cretaceous/Paleogene mass extinction for marine ecosystems. Annu Rev Ecol Evol Syst 36:295–317*
22. *de Vleeschouwer D, Da Silva AC, Boulvain F, Crucifix M, Claeys P (2012) Precessional and half-precessional climate forcing of Mid-Devonian monsoon-like dynamics. Clim Past 8:337–351. doi:10.5194/cp-8-337-2012*
23. *de Winter NJ, Zeeden C, Hilgen FJ (2014) Low-latitude climate variability in the Heinrich frequency band of the Late Cretaceous Greenhouse world. Clim Past 10:1001–1015. doi:10.5194/cp-10-1001-2014*
24. *Dessert C, Dupre B, Francois LM, Schott J, Gaillardet J, Chakrapani G, Bajpai S (2001) Erosion of Deccan Traps determined by river geochemistry: impact on the global climate and the Sr-87/Sr-86 ratio of seawater. Earth Planet Sci Lett 188:459–474*
25. *Edgar KM, Pälike H, Wilson PA (2013) Testing the impact of diagenesis on the $\delta^{18}O$ and $\delta^{13}C$ of benthic foraminiferal calcite from a sediment burial depth transect in the equatorial Pacific. Paleoceanography 28:468–480*

26. *Ellwood BB, Crick RE, Hassani AE, Benoist SL, Young RH (2000) Magnetosusceptibility event and cyclostratigraphy method applied to marine rocks: detrital input versus carbonate productivity. Geology 28:1135–1138*
27. *Erba E (1992) Calcareous nannofossil distribution in pelagic rhytmic sediments (Aptian–Albian Piobicco core, Central Italy). Riv Ital Paleontol Stratigr 97:455–484*
28. *Erba E, Castradori D, Guasti G, Ripepe M (1992) Calcareous nannofossils and Milankovitch cycles: the example of the Albian Gault Clay Formation (southern England). Palaeogeogr Palaeoclimatol 93:47–69*
29. *Erba E, Watkins D, Mutterlose J (1995) Campanian dwarf calcareous nannofossils from Wodejebato Gutyot. In: Haggerty JA, Premoli Silva I, Rack F, McNutt MK (eds) Proceedings of Ocean Drill Program. Sci Results 144:141–156*
30. *Eshet Y, Almogi-Labin A (1996) Calcareous nannofossils as paleoproductivity indicators in Upper Cretaceous organic-rich sequences in Israel. Mar Micropaleontol 29:37–61*
31. *Eshet Y, Moshkovitz S, Habib D, Benjamini C, Magaritz M (1992) Calcareous nannofossil and dinoflagellate stratigraphy across the Cretaceous/Tertiary boundary at Hor Hahar, Israel. Mar Micropaleontol 18:199–228*
32. *Fisher CG, Hay WW (1999) Calcareous nannofossils as indicators of Mid-Cretaceous paleofertility along an ocean front, U. S. Western Interior. In: Barrera E, Johnson CC (eds) Evolution of the Cretaceous ocean-climate system. Geol Soc Am 332:161–180*
33. *Friedrich O, Herrle JO, Hemleben C (2005) Climatic changes in the Late Campanian-Early Maastrichtian: micropaleontological and stable isotopic evidence from an epicontinental sea. J Foramin Res 35:228–247*
34. *Friedrich O., Herrle J.O., Wilson P.A., Cooper M.J., Erbacher J., Hemleben C. (2009) Early Maastrichtian carbon cycle perturbation and cooling event: implications from the South Atlantic Ocean. Paleoceanography 24, PA2211. doi:10.1029/2008PA001654*
35. *Gardin S (2002) Late Maastrichtian to early Danian calcareous nannofossils at Elles (Northwest Tunisia). A tale of one million years across the K–T boundary. Palaeogeogr Palaeoclimatol 178:211–231*
36. *Gardin S, Monechi S (1998) Palaeoecological change in middle to low latitude calcareous nannoplankton at the Cretaceous/Tertiary boundary. Bull Soc Geol Fr 169:709–723*
37. *Gardin S, Galbrun B, Thibault N, Coccioni R, Premoli-Silva I (2012) Bio-magnetochronology for the upper Campanian Maastrichtian from the Gubbio area, Italy: new results from the Contessa Highway and Bottaccione sections. Newsl Stratigr 45:75–103*
38. *Grinsted A, Moore JC, Jevrejeva S (2004) Application of the cross wavelet transform and wavelet coherence to geophysical time series. Nonlinear Process Geophys 11:561–566*
39. *Grossman EL (2012) Chapter 10: oxygen isotope stratigraphy. In: Gradstein FM et al (eds) The geologic time scale 2012. Elsevier, Boston, pp 181–206*
40. *Hagelberg TK, Bond G, deMenocal P (1994) Milankovitch band forcing of sub-Milankovitch climate variability during the Pleistocene. Paleoceanography 9:545–558*
41. *Hardas P, Mutterlose J (2007) Calcareous nannofossils assemblages of Oceanic Anoxic Event 2 in the equatorial Atlantic: evidence of an eutrophication event. Mar Micropaleontol 66:52–69*
42. *Hardas P, Mutterlose J, Friedrich O, Erbacher J (2012) The Middle Cenomanian Event in the equatorial Atlantic: the calcareous nannofossil and benthic foraminiferal response. Mar Micropaleontol 96–97:66–74*
43. *Hennebert M (2012) Hunting for the 405-kyr eccentricity cycle phase at the Cretaceous–Paleogene boundary in the Aïn Settara section (Kalaat Senan, central Tunisia). Carnets de Géologie [Notebooks on Geology], Brest, Article 2012/05 (CG2012_A05): 93–116*
44. *Henriksson AS (1993) Biochronology of the terminal Cretaceous calcareous nannofossil Zone of Micula prinsii. Cretac Res 14:59–68*

45. *Herbert TD (1999) Toward a composite orbital chronology for the Late Cretaceous and Early Palaeocene GPTS. Philos Trans R Soc Lond A 357:1891–1905*
46. *Herbert TD, Premoli Silva I, Erba E, Fischer AG (1995) Orbital Chronology of Cretaceous-Paleocene marine sediments, in: Geochronology Time Scales and Global Stratigraphic Correlation, SEPM Spec Pub, pp 80–93*
47. *Hermoso M, Le Callonnec L, Minoletti F, Renard M, Hesselbo SP (2009) Expression of the Early Toarcian negative carbon-isotope excursion in separated carbonate microfractions (Jurassic, Paris Basin). Earth Planet Sci Lett 277:194–203*
48. *Hill ME (1975) Selective dissolution of Mid-Cretaceous (Cenomanian) Calcareous Nannofossils. Micropaleontology 21:227–235*
49. *Hinnov LA (2000) New perspectives on orbitally forced stratigraphy. Annu Rev Earth Planet Sci 28:419–475*
50. *Hull PM, Norris RD, Bralower TJ, Schueth JD (2011) A role for chance in marine recovery from the end-Cretaceous extinction. Nat Geosci 4:856–860*
51. *Husson D, Galbrun B, Laskar J, Hinnov LA, Thibault N, Gardin S, Locklair RE (2011) Astronomical calibration of the Maastrichtian (Late Cretaceous). Earth Planet Sci Lett 305:328–340*
52. *Husson D, Galbrun B, Gardin S, Thibault N (2014a) Tempo and duration of short-term environmental perturbations across the Cretaceous–Paleogene boundary. Stratigraphy (in press)*
53. *Husson D, Thibault N, Galbrun B, Gardin S, Minoletti F, Sageman B, Huret E (2014b) Lower Maastrichtian cyclostratigraphy of the Bidart section (Basque country, SW France): a remarkable record of precessional forcing. Palaeogeogr Palaeoclimatol 395:176–197*
54. *Jarvis I, Mabrouk A, Moody RTJ, de Cabrera S (2002) Late Cretaceous (Campanian) carbon isotope events, sea-level change and correlation of the Tethyan and Boreal realms. Palaeogeogr Palaeoclimatol 188:215–248*
55. *Jarvis I, Gale AS, Jenkyns HC, Pearce MA (2006) Secular variation in Late Cretaceous carbon isotopes: a new δ13C carbonate reference curve for the Cenomanian-Campanian (99.6–70.6 Ma). Geol Mag 143:561–608*
56. *Jenkyns HC, Mutterlose J, Sliter WV (1995) Upper Cretaceous carbon- and oxygen isotope stratigraphy of deep-water sediments from the North-Central Pacific (Site 869, Flank of Pikini-Wodejebato, Marshall Islands). Proc ODP Sci Res 143:105–108*
57. *Jiang S, Bralower TJ, Patzkowsky ME, Kump LR, Schueth JD (2010) Geographic controls on nannoplankton extinction across the Cretaceous/Palaeogene boundary. Nat Geosci 3:280–285*
58. *Jung C, Voigt S, Friedrich O, Koch MC, Frank M (2013) Campanian–Maastrichtian ocean circulation in the tropical Pacific. Paleoceanography 28:1–12. doi:10.1002/palo.20051*
59. *Keller G, Adatte T, Gardin S, Bartolini A, Bajpai S (2008) Main Deccan volcanism phase ends near the K–T boundary: evidence from the Krishna–Godavari Basin, SE India. Earth Planet Sci Lett 268:293–311*
60. *Keller G, Adatte T, Bhowmick P, Upadhyay H, Dave A, Reddy AN, Jaiprakash BC (2012) Nature and timing of extinctions in Cretaceous-Tertiary planktic foraminifera preserved in Deccan intertrappean sediments of the Krishna–Godavari Basin, India. Earth Planet Sci Lett 341–344:211–221*
61. *Kessels K, Mutterlose J, Michalzik D (2006) Early Cretaceous (Valanginian–Hauterivian) calcareous nannofossils and isotopes of the northern hemisphere: proxies for the understanding of Cretaceous climate. Lethaia 39:157–172*
62. *Kucera M, Malmgren BA (1998) Terminal Cretaceous warming event in the mid-latitude South Atlantic Ocean: evidence from poleward migration of Contusotruncana contusa (planktonic foraminifera) morphotypes. Palaeogeogr Palaeoclimatol 138:1–15*

63. *Kuiper KF, Deino A, Hilgen FJ, Krijgsman W, Renne PR, Wijbrans JR (2008) Synchronizing rock clocks of earth history. Science 320:500–504*
64. *Kump LR, Arthur MA (1999) Interpreting carbon-isotope excursions: carbonates and organic matter. Chem Geol 161:181–198*
65. *Laskar J, Robutel P, Joutel F, Gastineau M, Correia A, Levrard B (2004) A long term numerical solution for the insolation quantities of the earth. Astron Astrophys 428:261–285*
66. *Lees JA (2002) Calcareous nannofossil biogeography illustrates palaeoclimate change in the Late Cretaceous Indian Ocean. Cretaceous Res 23:537–634*
67. *Lees JA, Bown PR, Mattioli E (2005) Problems with proxies? Cautionary tales of calcareous nannofossils paleoenvironmental indicators. Micropaleontology 51:333–343*
68. *Li L, Keller G (1998a) Abrupt deep-sea warming at the end of the Cretaceous. Geology 26:995–998*
69. *Li L, Keller G (1998b) Maastrichtian climate, productivity and faunal turnovers in planktic foraminifera in South Atlantic DSDP sites 525A and 21. Mar Micropaleontol 33:55–86*
70. *Li L, Keller G, Adatte T, Stinnesbeck W (2000) Late Cretaceous sea-level changes in Tunisia: a multi-disciplinary approach. J Geol Soc Lond 157:447–458*
71. *Linnert C, Mutterlose J (2009) Evidence of increasing surface water oligotrophy during the Campanian–Maastrichtian boundary interval: Calcareous nannofossils from DSDP Hole 390A (Blake Nose). Mar Micropaleontol 73:29–36*
72. *Linnert C, Mutterlose J, Erbacher J (2010) Calcareous nannofossils of the Cenomanian/Turonian boundary interval from the Boreal Realm (Wunstorf, northwest Germany). Mar Micropaleontol 74:38–58*
73. *Linnert C, Mutterlose J, Herrle JO (2011) Late Cretaceous (Cenomanian–Maastrichtian) calcareous nannofossils from Goban Spur (DSDP Sites 549, 551): Implications for the palaeoceanography of the proto North Atlantic. Palaeogeogr Palaeoclimatol 299:507–528*
74. *Maurer F, Hinnov LA, Schlager W (2004) Statistical time-series analysis and sedimentological tuning of bedding rhythms in a Triassic basinal succession (Southern Alps, Italy). In: D'Argenio B et al (eds) Cyclostratigraphy: approaches and case histories, SEPM Spec Publ 81, pp 83–99*
75. *Minoletti F, de Rafélis M, Renard M, Gardin S (2004) Reworking of Maastrichtian-like calcareous nannofossils in the lowermost Danian sediments of Bidart section (France): isotopic evidence (carbon and oxygen). Rev Micropaléontol 47:145–152*
76. *Minoletti F, de Rafélis M, Renard M, Gardin S, Young J (2005) Changes in the pelagic fine fraction carbonate sedimentation during the Cretaceous-Paleocene transition: contributions of the separation technique to the study of Bidart section. Palaeogeogr Palaeoclimatol 216:119–137*
77. *Mitchell SF, Ball JD, Crowley SF, Marshall JD, Paul CRC, Veltkamp CJ, Samir A (1997) Isotope data from cretaceous chalks and foraminifera: environmental or diagenetic signals? Geology 25:691–694*
78. *Molina E, Alegret L, Arenillas I, Arz JA, Gallala N, Hardenbol J, von Salis K, Steurbaut E, Vandenberghe N, Zaghbib-Turki D (2006) The Global Stratotype Section and Point for the base of the Danian stage (Paleocene, Paleogene, "Tertiary", Cenozoic) at El Kef, Tunisia—original definition and revision. Episodes 29:263–273*
79. *Molina E, Alegret L, Arenillas I, Arz JA, Gallala N, Grajales-Nishimura JM, Murillo-Muñetón G, Zaghbib-Turki D (2009) The global stratotype section and point for the base of the Danian stage (Paleocene, Paleogene, "Tertiary", Cenozoic): auxiliary sections and correlations. Episodes 32:84–95*
80. *Moolna A, Rickaby REM (2012) Interaction of the coccolithophore Gephyrocapsa oceanica with its carbon environment: response to a recreated high-CO_2 geological past. Geobiology 10:72–81*

81. *Mutterlose J (1991) Das Verteilungs- und Migrationsmuster des kalkigen Nannoplanktons in der borealen Unterkreide (Valangin-Apt). Palaeontogr B 221:27–152*
82. *Mutterlose J (1992) Lower Cretaceous nannofossil biostratigraphy off northwestern Australia (Leg 123). In: Proceedings of Ocean Drill Program. Sci Results 123:343–368*
83. *Mutterlose J, Kessels K (2000) Early Cretaceous calcareous nannofossils from the high latitudes: implications for palaeobiogeography and palaeoclimate. Palaeogeogr Palaeoclimatol 160:347–372*
84. *Nordt LC, Atchley SC, Dworkin SI (2003) Terrestrial evidence for two greenhouse events in the latest Cretaceous. GSA today 13:4–9*
85. *Norris RD, Kroon D, Klaus A et al (1998) Shipboard scientific party. Proc ODP Init Rep 171B:11–44*
86. *Olsson RK, Wright JD, Miller KG (2001) Paleobiogeography of Pseudotextularia Elegans During the Latest Maastrichtian global warming event. J Foramin Res 31:275–282*
87. *Pardo A, Ortiz N, Keller G (1996) Latest Maastrichtian and K/T boundary foraminiferal turnover and environmental changes at Agost, Spain. In: MacLeod N, Keller G (eds) Biotic and environmental events across the Cretaceous/Tertiary boundary. GSA Spec Pap 307:139–171*
88. *Patterson RT, Fishbein E (1989) Re-examination of the statistical methods used to determine the number of point counts needed for micropaleontological quantitative research. J Paleontol 63:245–248*
89. *Perch-Nielsen K (1985) Mesozoic calcareous nannofossils. In: Bolli HM et al (eds) Plankton stratigraphy. Cambridge University Press, Cambridge, pp 329–426*
90. *Perch-Nielsen K, McKenzie J, He Q (1982) Biostratigraphy and isotope stratigraphy and the 'catastrophic' extinction of calcareous nannoplankton at the Cretaceous/Tertiary boundary. In: Silver LT, Schultz P (eds) Geological implications of impacts of large asteroids and comets on the Earth. GSA Spec Paper 190:353–371*
91. *Peypouquet JP, Grousset F, Mourguiart P (1986) Paleoceanography of the Mesogean Sea based on ostracods of the northern tunisian continental shelf between the Late Cretaceous and Early Paleogene. Geol Rundsch 75:159–174*
92. *Pospichal JJ (1996) Calcareous nannoplankton mass extinction at the Cretaceous/Tertiary boundary: An update. In: Ryder G et al (eds) The Cretaceous-Tertiary event and other catastrophes in Earth history. GSA Spec Paper 307:335–360*
93. *Premoli Silva I, Erba E, Tornaghi ME (1989) Paleoenvironmental signals and changes in surface fertility in Mid Cretaceous Corg-Rich pelagic facies of the Fucoid Marls (Central Italy). Geobios 22:225–236*
94. *Punekar J, Mateo P, Keller G (2014) Effects of Deccan volcanism on paleoenvironment and planktic foraminifera: a global survey. In: Keller G, Kerr AC (eds) Volcanism, impacts, and mass extinctions: causes and effects. GSA Spec Pap 505:91–116*
95. *Renne PR, Deino AL, Hilgen FJ, Kuiper KF, Mark DF, Mitchell WS, Morgan LE, Mundil R, Smit J (2013) Time scales of critical events around the Cretaceous–Paleogene boundary. Science 339:684–687*
96. *Reuning L, Reijmer JJG, Betzler C, Timmermann A, Steph S (2006) Sub-Milankovitch cycles in periplatform carbonates from the early Pliocene Great Bahama Bank. Paleoceanography 21:PA1017. doi:10.1029/2004PA001075*
97. *Rickaby REM, Henderiks J, Young JN (2010) Perturbing phytoplankton: response and isotopic fractionation with changing carbonate chemistry in two coccolithophore species. Clim Past 6:771–785*
98. *Robinson N, Ravizza G, Coccioni R, Peucker-Ehrenbrink B, Norris R (2009) A high-resolution marine 187Os/188 Os record for the late Maastrichtian: distinguishing the chemical fingerprints of Deccan volcanism and the KP impact event. Earth Planet Sci Lett 281:159–168*

99. *Rodriguez-Tovar FJ, Pardo-Iguzquiza E (2003) Strong evidence of high-frequency (sub-Milankovitch) orbital forcing by amplitude modulation of Milankovitch signals. Earth Planet Sci Lett 210:179–189*
100. *Roth PH, Krumbach KR (1986) Middle Cretaceous calcareous nannofossil biogeography and preservation in the Atlantic and Indian oceans: implications for paleoceanography. Mar Micropaleontol 10:235–266*
101. *Said R (1978) Etude Stratigraphique et micropaléontologique du passage Crétacé-Tertiaire du synclinal d'Elles (Région Siliana-Sers), Tunisie centrale. Université Pierre et Marie Curie, Paris 6, France*
102. *Schoene B, Samperton KM, Eddy MP, Keller G, Adatte T, Bowring SA, Khadri SFR, Gertsch B (2015) U-Pb geochronology of the Deccan Traps and relation to the end-Cretaceous mass extinction. Science 347(6218):182184. doi:10.1126/science.aaa0118*
103. *Schulte P et al (2010) The Chicxulub asteroid impact and mass extinction at the Cretaceous–Paleogene boundary. Science 327:1214–1218*
104. *Schulz M, Mudelsee M (2002) REDFIT: estimating red-noise spectra directly from unevenly spaced paleoclimatic time series. Comput Geosci 28:421–426*
105. *Self S, Blake S, Sharma K, Widdowson M, Sephton S (2008) Sulfur and chlorine in Late Cretaceous Deccan magmas and eruptive gas release. Science 319:1654–1657*
106. *Sheldon E, Ineson J, Bown P (2010) Late Maastrichtian warming in the Boreal Realm: Calcareous nannofossil evidence from Denmark. Palaeogeogr Palaeoclimatol 295:55–75*
107. *Stinnesbeck W, Ifrim C, Salazar C (2012) The Last Cretaceous Ammonites in Latin America. Acta Palaeontol Pol 57:717–728*
108. *Stüben D et al (2003) Late Maastrichtian paleoclimatic and paleoceanographic changes inferred from Sr/Ca ratio and stable isotopes. Palaeogeogr Palaeoclimatol 199:107–127*
109. *Sun J, Huang X (2006) Half-precessional cycles recorded in Chinese loess: response to low-latitude insolation forcing during the Last Interglaciation. Quat Sci Rev 25:1065–1072*
110. *Taner MT (2000) Attributes revisited. Technical Publication, Rock Solid Images, Houston. http://www.rocksolidimages.com/pdf/attrib_revisited.htm*
111. *Tantawy AAAM (2003) Calcareous nannofossil biostratigraphy and paleoecology of the Cretaceous-Tertiary transition in the central eastern desert of Egypt. Mar Micropaleontol 47:323–356*
112. *Tantawy AAAM (2008) Calcareous nannofossil biostratigraphy and paleoecology of the Cenomanian–Turonian transition in the Tarfaya Basin, southern Morocco. Cretaceous Res 29:995–1007*
113. *Thibault N, Gardin S (2006) Maastrichtian calcareous nannofossil biostratigraphy and paleoecology in the Equatorial Atlantic (Demerara Rise, ODP Leg 207 Hole 1258A). Rev Micropaléontol 49:199–214*
114. *Thibault N, Gardin S (2007) The late Maastrichtian nannofossil record of climate change in the South Atlantic DSDP Hole 525A. Mar Micropaleontol 65:163–184*
115. *Thibault N, Gardin S (2010) The calcareous nannofossil response to the end-Cretaceous warm event in the Tropical Pacific. Palaeogeogr Palaeoclimatol 291:239–252*
116. *Thibault N, Harlou R, Schovsbo N, Schiøler P, Minoletti F, Galbrun B, Lauridsen BW, Sheldon E, Stemmerik L, Surlyk F (2012a) Upper Campanian–Maastrichtian nannofossil biostratigraphy and high-resolution carbon-isotope stratigraphy of the Danish Basin: towards a standard δ13C curve for the Boreal Realm. Cretaceous Res 33:72–90*
117. *Thibault N, Husson D, Harlou R, Gardin S, Galbrun B, Huret E, Minoletti F (2012b) Astronomical calibration of upper Campanian-Maastrichtian carbon isotope events and calcareous plankton biostratigraphy in the Indian Ocean (ODP Hole 762C): implication for the age of the Campanian–Maastrichtian boundary. Palaeogeogr Palaeoclimatol 337–338:52–71*

118. *Thierstein HR (1980) Selective dissolution of late cretaceous and earliest tertiary calcareous nannofossils: experimental evidence. Cretaceous Res 1:165–176*
119. *Thierstein HR (1981) Late Cretaceous nannoplankton and the change at the Cretaceous/Tertiary boundary. SEPM Spec Publ 32:355–394*
120. *Thomson DJ (1982) Spectrum estimation and harmonic analysis. Proc IEEE 70:1055–1096*
121. *Tiraboschi D, Erba E, Jenkyns HC (2009) Origin of rhythmic Albian black shales (Piobicco core, central Italy): Calcareous nannofossils quantitative and statistical analyses and paleoceanographic reconstructions. Paleoceanography. doi:10.1029/2008PA001670*
122. *Tobin TS, Ward PD, Steig EJ, Olivero EB, Hilburn IA, Mitchell RN, Diamond MR, Raub TD, Kirschvink JL (2012) Extinction patterns, δ18O trends, and magnetostratigraphy from a southern high-latitude Cretaceous-Paleogene section: links with Deccan volcanism. Palaeogeogr Palaeoclimatol 350–352:180–188*
123. *Tobin TS, Wilson GP, Eiler JM, Hartman JH (2014) Environmental change across a terrestrial Cretaceous–Paleogene boundary section in eastern Montana, USA, constrained by carbonate clumped isotope paleothermometry. Geology. doi:10.1130/G35262.1*
124. *Tuenter E, Weber SL, Hilgen FJ, Lourens LJ (2003) The response of the African summer monsoon to remote and local forcing due to precession and obliquity. Global Planet Change 36:219–235*
125. *Tuenter E, Weber SL, Hilgen FJ, Lourens LJ (2007) Simulating sub-Milankovitch climate variations associated with vegetation dynamics. Clim Past 3:169–180. doi:10.5194/cp-3-169-2007*
126. *Voigt S, Gale AS, Jung C, Jenkyns HC (2012) Global correlation of Upper Campanian–Maastrichtian successions using carbon-isotope stratigraphy: development of a new Maastrichtian timescale. Newslett Stratigr 45:25–53*
127. *Voigt S, Jung C, Friedrich O, Frank M, Teschner C, Hoffmann J (2013) Tectonically restricted deep-ocean circulation at the end of the Cretaceous greenhouse. Earth Planet Sci Lett 369–370:169–177*
128. *Ward PD (1990) A review of Maastrichtian ammonite ranges. In: Sharpton VL, Ward PD (eds) Global catastrophes in earth history: an international conference on impacts, volcanism and mass mortality. GSA Spec Pap 247:519–530*
129. *Watkins DK, Self-Trail JM (2005) Calcareous nannofossil evidence for the existence of the Gulf Stream during the late Maastrichtian. Paleoceanography. doi:10.1029/2004PA001121*
130. *Watkins DK, Wise SW Jr, Pospichal JJ, Crux J (1996) Upper Cretaceous calcareous nannofossil biostratigraphy and paleoceanography of the Southern Ocean. In: Moguilevsky A, Whatley RC (eds) Microfossils and oceanic environments. University of Wales, Aberystwyth-Press, United Kingdom, pp 355–381*
131. *Weedon GP (2003) Time-Series Analysis and Cyclostratigraphy. Cambridge University Press, Cambridge*
132. *Wendler I (2013) A critical evaluation of carbon isotope stratigraphy and biostratigraphic implications for Late Cretaceous global correlation. Earth Sci Rev 126:116–146*
133. *Westerhold T, Röhl U, Raffi I, Fornaciari E, Monechi S, Reale V, Bowles J, Evans HF (2008) Astronomical calibration of the Paleocene time. Palaeogeogr Palaeoclimatol 257:377–403*
134. *Wignall PB (2001) Large igneous provinces and mass extinctions. Earth Sci Rev 53:1–33*

135. *Wilf P, Johnson KR, Huber BT (2003) Correlated terrestrial and marine evidence for global climate changes before mass extinction at the Cretaceous–Paleogene boundary. Proc Natl Acad Sci USA 100:599–604*
136. *Williams JR, Bralower TJ (1995) Nannofossil assemblages, fine fraction stable isotopes, and the paleoceanography of the Valanginian–Barremian (Early Cretaceous) North Sea Basin. Paleoceanography 10:815–839*
137. *Wu H, Zhang S, Feng Q, Jiang G, Li H, Yang T (2012) Milankovitch and sub-Milankovitch cycles of the early Triassic Daye Formation, South China and their geochronological and paleoclimatic implications. Gondwana Res 22:748–759*
138. *Zaghbib-Turki D, Karoui-Yaakoub N, Rocchia R, Robin E, Belayouni H (2000) Enregistrement des événements remarquables de la limite Crétacé-Tertiaire dans la coupe d'Ellès (Tunisie). CR Acad Sci IIA 331:141–149*